Effects of forest cover, topography, and sampling extent on the measured density of shallow, translational landslides

Daniel J. Miller[1] and Kelly M. Burnett[2]

Received 13 December 2005; revised 4 October 2006; accepted 1 November 2006; published 23 March 2007.

[1] We use regionally available digital elevation models and land cover data, calibrated with ground- and photo-based landslide inventories, to produce spatially distributed estimates of shallow, translational landslide density (number/unit area). To discern effects of land use, we focus on resolving landslide density relationships with forest cover. We account for topographic variability between sites and landslide detection bias in air photo mapping. Even so, for sites in the Oregon Coast Range, we find great variability in the ratios of landslide density in forest classes among sites. We present strategies for subsampling available data to quantify this variability. For these data, we find that older forests, when sampled over tens of square kilometers, commonly exhibited the highest landslide densities but over hundreds of square kilometers always exhibited the lowest densities, averaging 30% of that in recently harvested areas and 79% of that in younger, managed forests.

Citation: Miller, D. J., and K. M. Burnett (2007), Effects of forest cover, topography, and sampling extent on the measured density of shallow, translational landslides, *Water Resour. Res.*, *43*, W03433, doi:10.1029/2005WR004807.

1. Introduction

[2] Landslides are an important process for sediment delivery to mountain streams [*Hovius et al.*, 2000; *Kelsey*, 1980]. In forested terrain, timber harvest and road building can alter landslide characteristics [*Montgomery et al.*, 2000; *Swanson and Dyrness*, 1975], with potentially adverse effects on aquatic ecosystems. Degradation of aquatic habitat associated with increased landsliding [*Hartman et al.*, 1996; *Hicks et al.*, 1991] is a factor implicated in reducing, and even extirpating, culturally and economically important populations of Pacific salmon and trout [*Nehlsen et al.*, 1991]. This has motivated interest in examining effects of land management on landslide processes [*Collins and Pess*, 1997; *Dunne*, 1998] and spurred federal and state agencies to assess and monitor landslide occurrences [*Bush et al.*, 1997; *Robison et al.*, 1999] with consequent regulatory constraints to limit human influences on landsliding [*Oregon Department of Forestry*, 2006; *U.S. Department of Agriculture and U.S. Department of the Interior*, 1994; *Washington Department of Natural Resources*, 2005].

[3] Although any type of landslide can affect stream channels, here we focus on landslides that are likely to initiate debris flows, specifically rainfall-triggered translational landsliding of shallow soils [*Iverson et al.*, 1997]. Debris flows are of particular importance because they can travel long distances to and through stream channels [*Benda and Cundy*, 1990]. By creating a debris flow, a small landslide can affect stream channels far downslope, both by scouring accumulated soil and organic debris from steep, low-order channels [*May and Gresswell*, 2003] and by depositing the scoured material into larger, fish-bearing streams [*May and Gresswell*, 2004]. Landslide-triggered debris flows thus play two important and related roles in river environments. One is creation of persistent geomorphic features: their deposits create distinct valley floor fan and terrace landforms [*Benda*, 1990; *Miller and Benda*, 2000; *Wohl and Pearthree*, 1991]. The other is dynamic: they link forest disturbances, which can increase landslide susceptibility [*Schmidt et al.*, 2001], to downslope stream and riparian disturbances [*Cenderelli and Kite*, 1998; *Gomi et al.*, 2002; *Miller*, 1990; *Nakamura et al.*, 2000]. Together, these persistent and transient debris flow influences affect the spatial and temporal distribution of habitat and biota in mountain river networks [*Benda et al.*, 2004; *Lamberti et al.*, 1991; *Montgomery*, 1999; *Pabst and Spies*, 2001; *Rice et al.*, 2001] and both must be recognized to anticipate effects of land management in these aquatic ecosystems [*Reeves et al.*, 1995].

[4] A first step in efforts to discern land management effects on debris flow influences to regional ecosystems is identification of sites susceptible to debris flow initiation and assessment of forest disturbance on the degree of susceptibility. Topographic attributes (i.e., slope gradient and convergence) are recognized as primary factors controlling susceptibility of shallow soils to landsliding [*Chen and Jan*, 2003; *Hack and Goodlett*, 1960; *Niemann and Howes*, 1991; *Reneau et al.*, 1990]. Hillslope topography thus sets the stage for the spatial distribution of debris flow effects. Overprinted on the topographic template is the modulating influence of forest cover, acting through root reinforcement [*Burroughs and Thomas*, 1977; *Schmidt et al.*, 2001] and perhaps also through smoothing of rainfall intensity [*Keim and Skaugset*, 2003], on the initiation of shallow landsliding [*May*, 2002; *Montgomery et al.*, 2000; *Sidle and Ochiai*, 2006; *Swanson and Dyrness*, 1975].

[1] Earth Systems Institute, Seattle, Washington, USA.
[2] Pacific Northwest Research Station, Forest Service, U.S. Department of Agriculture, Corvallis, Oregon, USA.

0043-1397/07/2005WR004807$09.00

[5] Spatial variability in landslide susceptibility is influenced by topographic and forest cover characteristics at a relatively fine spatial resolution (of order 10^2 m^2); however, land management and conservation planning decisions for many stream-dwelling species, particularly salmon and trout, can benefit from knowledge of landslide susceptibility across large spatial extents (of order 10^5 km^2). Spatial variability in landslide susceptibility is also affected by variability in numerous factors other than topography and forest cover [*Dunne*, 1998]. These include variability in site conditions, such as soil depth and geotechnical properties [*Hammond et al.*, 1992; *Wu*, 1996] and spatiotemporal variability in landslide triggers, such as rainfall intensity [*Mark and Newman*, 1988]. Data are typically lacking to explicitly address these other pertinent factors in high-resolution, regionally applicable models of landslide susceptibility. Therefore a modeling approach that minimizes sensitivity of results to spatial variability in these factors while capitalizing on widely available 10-m digital elevation models (DEMs) [*Gesch et al.*, 2002] and forest cover mapping from satellite imagery could be of great value.

[6] One approach is to empirically associate mapped landslide initiation sites with topographic and forest cover characteristics [e.g., *Coe et al.*, 2004; *May*, 2002]. Field surveys and interpretation of aerial photography are common sources of landslide mapping. However, each source presents problems for use in regional modeling of landslide susceptibility. Inventories from field surveys can reasonably include only relatively small areas, yielding landslide counts or densities by forest cover class that may vary substantially from site to site [*Robison et al.*, 1999]. In contrast, inventories from aerial photographs may include a larger area to discern regional trends in the relative density of landslides between forest cover classes, but small landslides are more visible in unforested areas on aerial photographs, which introduces bias in landslide counts between forest cover classes [*Brardinoni et al.*, 2003; *Pyles and Froehlich*, 1987]. Weaknesses in each type of inventory can be overcome by combining information from the two sources. The proportion of small landslides missed in an air photo inventory can be estimated from landslide size distributions from a field inventory. Consequently, the air photo inventory can be used to evaluate variations in landslide density as a function of the area over which it is measured and to estimate uncertainty in measured values.

[7] In this paper, we describe methods to identify and characterize initiation sites of rainfall-triggered translational landslides in shallow soils and then demonstrate these methods for areas in the Oregon Coast Range, USA. Our objectives are to (1) characterize topographic influences on landslide density (in terms of number per unit area) using regionally available, high-resolution (10-m) DEMs; (2) specify methods to estimate, and potentially reduce, bias between different forest cover classes in counts of landslide initiation points mapped on aerial photographs; (3) determine ratios in densities of landslide initiation points between forest cover classes when corrected for bias from variable topography and air photo interpretation; and (4) evaluate variability in densities of landslide initiation points between different forest cover classes measured over a range of spatial extents. We also use these techniques to account for effects of forest roads on landslide density. Although results from this study are based on observations that span only a portion of the Oregon Coast Range, they provide the means to extrapolate a spatially distributed estimate of landslide susceptibility across the entire region. Additionally, the methods are readily applied with similar data elsewhere and the results offer insights for interpreting and designing other studies.

2. Methods

2.1. Overview

[8] Research spanning decades has guided development of conceptual and empirical models of landslide occurrence in mountain environments [see reviews by, e.g., *Dunne*, 1998; *Guzzetti et al.*, 1999; *Sidle et al.*, 1985; *Swanson et al.*, 1987]. Terrain attributes may be associated with measures of landslide susceptibility based on geomorphic mapping and professional judgment [*Wieczorek*, 1984], a quantitative statistical assessment relating attribute values with landslide locations [*Brenning*, 2005; *Guzzetti et al.*, 2000; *Soeters and van Westen*, 1996], or a combination of these [*Rollerson et al.*, 2002; *van Westen et al.*, 2003]. We take the second approach and seek to empirically relate the probability of encountering a mapped landslide initiation point within any specified area as a function of topographic and forest cover attributes, to the degree possible with regionally available data. This probability provides a measure of susceptibility. Landslide density provides a natural metric from which to infer spatial probability. We derive methods to fully capitalize on the spatial resolution of available topographic data, while still incorporating information from lower-resolution data on forest cover and geology.

[9] We characterize topographic influences in terms of a topographic weighting, which indicates the degree to which local topography, resolved over DEM pixel length, alters mean landslide density. We then estimate the appropriate landslide density to apply for different forest cover classes. This approach benefits from the higher resolution of available topographic data, but relies on the assumption that the relative effects of topography are the same for each forest cover class and also for other factors, such as geology. This is the simplest and most easily implemented scenario; we will examine the implications of this assumption using data from the Oregon Coast Range.

[10] We find the applicable landslide density for different forest cover classes by counting the landslides and measuring the area in each class. Use of a topographic weighting term allows us to account for differences in topography between different mapping units, so that if one forest class is situated on steeper slopes than another, for example, the influence of the steeper slopes can be removed. We are particularly interested in the relative difference in landslide density between different forest cover classes so that we can assess the aggregate effects of timber harvest on landslide susceptibility. For this purpose, the magnitude of the measured landslide densities is immaterial; it is the relative difference in density between forest cover classes that is important. We seek values to apply regionally, yet regional studies may indicate a large range in landslide densities and the forest cover classes with the highest and lowest densities are in some cases inconsistent from site to site [*Robison et*

al., 1999]. Reasons for such variability include unresolved or unaccounted for variability in site conditions, such as topography, soil properties, and tree spacing [*Dengler et al.*, 1987; *Dunne*, 1998; *Roering et al.*, 2003]. We expect, however, that there is some spatial extent over which variability from these sources can be averaged out and a persistent trend in the ratio of densities between forest cover classes identified [*Miller et al.*, 2003]. Evaluation of this hypothesis requires a large sample area, necessitating landslide mapping from aerial photographs, which introduces a source of bias in landslide counts between forest cover classes [*Brardinoni et al.*, 2003; *Pyles and Froehlich*, 1987].

[11] Spatiotemporal variability in landslide triggers, particularly rainfall intensity [*Mark and Newman*, 1988], can also create variability in measures of relative landslide density. In general, there are few data sources to evaluate this source of variability. If variations in rainfall intensity typically occur over spatial extents greater than variations in forest patch size (e.g., a harvest unit, which typically spans on the order of 10^1 hectares), then the ratio in landslide density between forest cover classes should be relatively consistent, even though rainfall intensities associated with landslide-triggering storms may vary dramatically across a region.

2.2. Topographic Influences on Landslide Density

2.2.1. Topographic Index

[12] Landslide-initiated debris flows are associated with rainfall-triggered failure of shallow soils in specific topographic locations. These landslides are generally confined to steep slopes [*Chen and Jan*, 2003; *Sidle et al.*, 1985] and tend to occur in topographic hollows [*Dietrich and Dunne*, 1978; *Hack and Goodlett*, 1960; *Reneau et al.*, 1990], although soil failures on planar slopes also occur [e.g., *May*, 2002]. These and other studies point to slope gradient, topographic convergence, and contributing area as potentially important topographic factors. We therefore choose a topographic index (I_T) that is a function of these attributes. This index is calculated for each pixel of the DEM. Mapped landslide initiation points are then overlain to obtain a cumulative frequency distribution of landslide points for the index function. We use this distribution to derive a topographic weighting term (w_T) to estimate local topographic influences on landslide density.

[13] The basis for a topographic index was a model presented by *Montgomery and Dietrich* [1994] that includes the attributes we were interested in to characterize topography. Although the model also contains variables to parameterize soil properties, we used only the topographic factors. This does not imply that soil properties are unimportant in determining landslide locations, only that data are not available to characterize their spatial variability, whereas data are available to characterize topographic variability. The model [*Montgomery and Dietrich*, 1994] is a simple representation of slope failure that assumes steady state hydrology and uses topographic factors of slope gradient and contributing area per unit contour width. The model is derived from the infinite slope approximation for failure of a thin soil overlying a more competent and less permeable substrate, with the assumption of surface-parallel flow of soil pore water in the saturated zone. *Iverson* [2000] raises objections to these assumptions for groundwater flow and presents an alternative, dynamic model for rainfall-triggered soil failure. In both cases, the important topographic variables are slope gradient and some measure of the area contributing to subsurface flow. The *Montgomery and Dietrich* [1994] model has been shown effective at identifying landslide-prone locations at sites throughout the Pacific Northwest and elsewhere [*Borga et al.*, 2002; *Dietrich et al.*, 2001; *Montgomery et al.*, 1998].

[14] With the assumptions stated above, conditions for failure of a cohesionless soil occur at a critical steady state rainfall intensity q_{cr} given by [*Montgomery and Dietrich*, 1994, equation (5)]

$$q_{cr} = \left[\frac{T \sin\theta\left(\rho_S/\rho_W\right)}{a/b}\right]\left[1 - \frac{\tan\theta}{\tan\phi}\right], \tag{1}$$

where T is soil transmissivity, θ is gradient of the ground surface, ρ_S is wet bulk density of the soil, ρ_W is the density of water, a is the area contributing subsurface flow across a soil column of width b perpendicular to the flow direction, and ϕ is the friction angle of the soil. By holding all soil parameters constant, equation (1) becomes a function solely of the topographic variables θ and a/b, and serves as a topographic index, i.e., $I_T = q_{cr}$ with T, ρ_S/ρ_W, and $\tan\phi$ held constant. Using a ϕ value of 45 degrees, we have

$$I_T = C \sin\theta\left(\frac{a}{b}\right)^{-1}(1 - \tan\theta), \tag{2}$$

where $C = T(\rho_S/\rho_W)$, which can be set to a constant value appropriate for soils in the area of interest, so that values from equation (2) can be compared with those from other studies using *Montgomery and Dietrich*'s [1994] model, or simply set to unity and ignored. For slopes steeper than 45 degrees, equation (2) gives negative index values. For plotting purposes (e.g., use of a logarithmic scale), we translated negative I_T values to positive values via the equation $0.1/(1 + 0.1 - I_T)$.

[15] To calculate contributing area a, we use the $D\infty$ flow direction algorithm described by *Tarboton* [1997], which allows downslope dispersion. The $D\infty$ algorithm calculates flow direction for a pixel using each of eight triangular facets defined by a DEM grid point and the eight adjacent points. For each facet having flow out of the pixel, we use the projection of flow direction on the exterior facet edge as a measure of contour length crossed by flow exiting the pixel from that facet. These projection lengths are summed over all edges with outgoing flow to provide an estimate of contour length b for flow exiting the pixel. Contour length for planar flow is one pixel width, for divergent flow it is greater than one pixel width, and for convergent flow it is less than one pixel width. The specific contributing area, a/b, thus incorporates effects of topographic convergence.

2.2.2. Topographic Weighting

[16] The correlation between the topographic index and landslide locations was obtained empirically on the basis of the index values found where landslides occurred. We express this correlation as a topographic weighting term. Because it is calibrated, the weighting is independent of the soil parameters used in equation (2).

[17] We expect the frequency distribution of topographic index values associated with landslide initiation points to differ from the frequency distribution of index values over the DEM as a whole. For the index defined in equation (2),

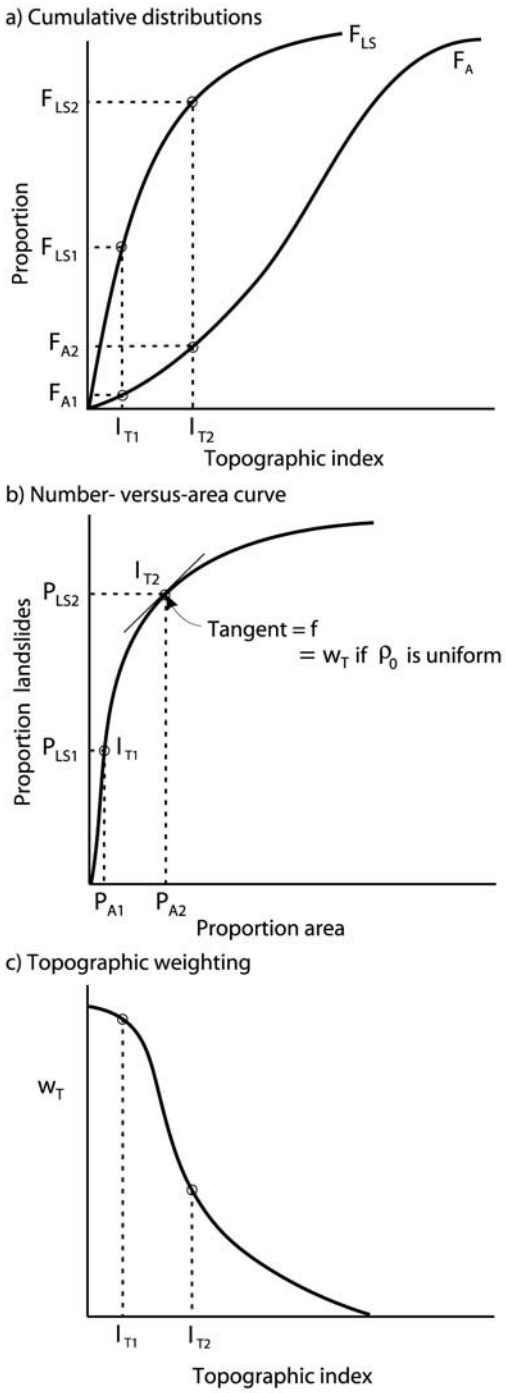

Figure 1. Illustrative sketches showing (a) cumulative distribution functions, equations (3) and (4), for landslides (F_{LS}) and DEM area (F_A) as functions of topographic index I_T; (b) number-versus-area curve derived from the cumulative distribution functions (points labeled I_{T1} and I_{T2} correspond to similarly labeled points in the cumulative distributions); the tangent at any point along the curve gives the value of function f, equation (5); and (c) the topographic weighting term, from equations (5) and (11), obtained from the tangent along the number-versus-area curve as a function of the topographic index.

we expect that landslides are preferentially associated with small index values, which represent steeper sites with larger specific contributing area, whereas we expect only a small proportion of DEM area to occupy these small-index-value locations. The likelihood ratio quantifies this relationship [*Coe et al.*, 2004; *Wieczorek et al.*, 1988]: for a given range of index values, the proportion of landslides divided by the proportion of DEM area provides a normalized measure of landslide density that varies with the topographic index. This ratio serves as a measure of landslide susceptibility [*Chung and Fabbri*, 2005].

[18] An index value, I_T from equation (2), can be calculated for every pixel of the DEM and overlain with digitized landslide initiation points. Empirical cumulative distribution functions are then constructed for landslides and for DEM area, giving the proportion of landslides and DEM pixels with an I_T value less than or equal to a specified limit (Figure 1a):

$$F_{LS}(x) = n_{LS}(x)/N_{LS} \tag{3}$$

$$F_A(x) = n_A(x)/N_A, \tag{4}$$

where F_{LS} is the cumulative distribution function for landslides, $n_{LS}(x)$ is the number of pixels containing a landslide initiation point with I_T values less than or equal to x, and N_{LS} is the total number of landslide initiation points. Similarly, F_A is the cumulative distribution function for DEM area; $n_A(x)$ is the number of pixels with I_T values less than or equal to x, and N_A is the total number of pixels in the DEM. Because we are interested in landslide initiation points, we associate each landslide in an inventory with a single pixel. However, both F_{LS} and F_A may be defined in terms of area (in which case landslide density would be defined as landslide area per unit area):

$$F_{LS}(x) = \big(a_p\, n_{LS}(x)\big)/\big(a_p\, N_{LS}\big)$$

$$F_A(x) = \big(a_p\, n_A(x)\big)/\big(a_p\, N_A\big),$$

where a_p is the area of a single pixel and both n_{LS} and N_{LS} refer to pixels encompassed by mapped landslide scars.

[19] Plotting F_{LS} against F_A shows the proportion of DEM area required to encompass a given proportion of the mapped landslide initiation points (Figure 1b). The F_{LS} versus F_A (number versus area) curve provides a measure of the extent to which landslide initiation locations are resolved by the topographic index with the elevation and landslide-mapping data used. It also defines a weighting function for landslide density. For a given small increment ΔI_T there are corresponding changes ΔF_{LS} and ΔF_A that determine the rate of change (the tangent, Figure 1b) along the F_{LS} versus F_A curve. We refer to this rate of change as f, a function of I_T given by

$$f(x) = \frac{\left(\Delta F_{LS}(x)\Big/\Delta I_T\right)}{\left(\Delta F_A(x)\Big/\Delta I_T\right)} = \frac{N_A}{N_{LS}} \frac{\left(\Delta n_{LS}(x)\Big/\Delta I_T\right)}{\left(\Delta n_A(x)\Big/\Delta I_T\right)} = \rho_0^{-1} \frac{\Delta n_{LS}(x)}{\Delta n_A(x)}. \tag{5}$$

Here ρ_0 is the mean landslide density (the number of landslides divided by the total number of pixels), and Δn_A

is the number of pixels and Δn_{LS} is the number of landslide initiation point pixels with I_T values in the increment $x \pm \Delta I_T/2$. From equation (5) we have

$$\Delta n_{LS}(x) = \rho_0 f(x) \Delta n_A(x), \tag{6}$$

the number of landslides associated with an increment ΔI_T is equal to the mean density times the area (in terms of DEM pixels) with area adjusted by the value of f at $I_T = x$, which increases the effective area for landslide-prone terrain, thus giving a larger number of landslides with equation (6), and decreases the effective area for stable terrain. In the limit, as ΔI_T approaches zero (or as pixel size approaches zero), equation (5) is expressed as a differential:

$$f(I_T) = \rho_0^{-1}(dn_{LS}/dn_A), \tag{7}$$

where we have eliminated the dummy variable x and allowed both n_{LS} and n_A to represent an infinitesimal portion of a pixel. The differential, dn_{LS}/dn_A, indicates the change in the number of landslides associated with a change in area for a given I_T value, from which the number of landslides is found by integrating over area. The fractional number of landslides associated with a single pixel is:

$$\delta n_{LS} = \rho_0 f_p,$$

where the pixel value f_p is the value of $f(I_T)$ calculated using the I_T value of the pixel. Thus the number of landslides expected over any arbitrary portion of a DEM is calculated as a sum over pixels:

$$\Delta n_{LS} = \sum (\rho_0 f_p). \tag{8}$$

The weighting function $f(I_T)$, obtained from the empirical cumulative distribution functions for landslides and DEM area ranked by topographic index, provides a pixel-by-pixel adjustment f_p that accounts for effects of topography on landslide density (Figure 1c). If summed over all pixels, equation (8) must give N_{LS}, the total number of landslides, which with the definition of mean landslide density ($\rho_0 = N_{LS}/N_A$), indicates that

$$\sum_{N_A} f_p = N_A \tag{9}$$

or that the mean value of f_p over the DEM of a study area used for calibration must equal one.

[20] Factors other than topography are incorporated into ρ_0, the mean landslide density. The mean density may be defined as an average over the study area or may be used to resolve differences between specific portions of the area delineated by mapping units for forest cover and, for example, rock type. To accommodate differences in density between these areas, we write equation (5) as

$$f(x) = \rho_0^{-1} \frac{\sum \left(\Delta n_{LSi}(x) \Big/ \Delta I_T \right)}{\sum \left(\Delta n_{Ai}(x) \Big/ \Delta I_T \right)} = \rho_0^{-1} \frac{\sum \left[f_i(x) \rho_i \left(\Delta n_{Ai}(x) \Big/ \Delta I_T \right) \right]}{\left(\frac{\Delta n_A(x)}{\Delta I_T} \right)}. \tag{10}$$

Here the subscript in the sums refers to the ith map unit of the DEM (e.g., a specific forest cover class), equation (6) was substituted for Δn_{LSi}, and the numerator reflects the sum of Δn_A over all map units. If topographic influences are invariant over all map units, then $f(x)$ will be the same for all of them, i.e., $f_i(x) = f_j(x) = w_T(x)$ for all map units i and j, $i \neq j$, and we can use equation (10) to correct for the effect of variations in mean landslide density on function f. Using w_T to refer to the corrected value, f_i in equation (10), and moving it outside the sum, we define

$$w_T(x) = f(x) \left(\frac{\rho_0 \left(\Delta n_A(x) \Big/ \Delta I_T \right)}{\sum \rho_i \left(\Delta n_{Ai}(x) \Big/ \Delta I_T \right)} \right). \tag{11}$$

Then w_T provides a composite weighting term, applicable to the entire DEM, used to weight mean landslide density to account for local topographic influences. If a single landslide density ρ_0 applies over the entire area, equation (11) reduces to equation (5). In the limit, as ΔI_T approaches zero, the change in area associated with a small change in I_T can be expressed as a differential:

$$w_T(I_T) = f(I_T) \left(\frac{\rho_0 \left(dn_A \Big/ dI_T \right)}{\sum \rho_i \left(dn_A \Big/ dI_T \right)_i} \right), \tag{12}$$

and w_T can be calculated for each pixel on the basis of the pixel I_T value. The term in the large parentheses adjusts the value of the empirical function $f(I_T)$ to account for variable mean landslide densities across the area covered by the DEM.

[21] If we compare two map units delineated by different forest cover classes, one encompassing steep, highly dissected terrain and the other lower-gradient, smoother terrain, the densities obtained by dividing landslide numbers by area may primarily reflect differences in topography, not forest cover. Equation (12), together with the definition of n_{LS} given above, provides a means of accounting for topographic differences when estimating mean landslide density for each map unit:

$$n_{LSi} = \rho_i \sum w_T, \tag{13}$$

where the subscript refers to the ith map unit. The number of landslide initiation points, plotted against topographically weighted area (the summed w_T values), lie along a line intersecting the origin with a slope given by mean landslide density, or even more simply, $\rho_i = n_{LSi}/\sum w_T$: landslide density for the ith map unit is given by the number of pixels with landslide initiation points divided by the summed w_T values, which serve as a topographically adjusted measure of map unit area.

2.2.3. Evaluating the Topographic Weighting Term

[22] Landslide predictions can be evaluated by subsampling the landslide data, using some portion to calibrate the model and the rest to assess the results [*Chung and Fabbri*, 2003]. We would like to use all the data to estimate a level of confidence in the predictions. Repeated subsampling with replacement (a bootstrap sample) from the landslide data is one option [*Gershenfeld*, 1999] to estimate a

probability density distribution for the composite weighting term. Another alternative, which we use here, is to generate synthetic landslide inventories for Monte Carlo simulations from the composite weighting term (w_T).

[23] As a first-order approximation, we assume that landslide locations in any homogenous area (e.g., a map unit) are independent of each other and follow a Poisson distribution, from which the probability P_{LS} that a landslide initiation point was mapped in any DEM pixel is given by

$$P_{LS} = \frac{e^{-\rho_0 w_T a_p}\left(\rho_0 w_T a_p\right)}{1!} \approx \rho_0 w_T a_p, \tag{14}$$

where a_p is the area of a single pixel. For landslide densities ρ_0 of order 1 per km^2, $\rho_0 w_T a_p$ is of order 10^{-4} and $e^{-\rho_0 w_T a_p}$ is of order one. Hence the probability that any pixel contains a landslide initiation point is given approximately by $\rho_0 w_T a_p$. To generate a synthetic landslide inventory, we proceed pixel by pixel through the DEM, generating a sample from a uniform distribution between zero and one for each pixel. If the sample is less than the P_{LS} value for the pixel, we assign one landslide to that pixel. This generates a new set of landslide locations for the DEM consistent with the empirically calibrated topographic weighting term and mean density. We use this synthetic inventory to generate a new number-versus-area curve. Each synthetic inventory yields a different curve, all created with the same topographic weighting term. Repeated many times, this provides an approximate probability density distribution of number-versus-area curves. This simulation procedure indicates the range of variability expected for a given weighting term and a given DEM. We can compare the range of number-versus-area curves to the curve obtained for a set of mapped landslides. The degree to which the curve for the observed landslides falls within the expected range indicates how well the weighting term represents observed landslide locations.

[24] For simplicity, we are interested in applying a single composite topographic weighting term for all forest cover and geologic map units. Monte Carlo simulations applied over each set of map units separately show how well a single characterization of topographic influences applies in each case.

2.3. Detection Bias in an Air Photo–Based Landslide Inventory

[25] The proportion of landslides missed in photo mapping can be large and is influenced by a number of factors, including: photo scale, quality, and type (e.g., black and white or color); the shape, position and age of the landslide scars; and the experience of the photo interpreter [*Guzzetti et al.*, 2000]. Even if bias from these sources is minimized, some landslides under forest cover may be hidden by shadow and tree canopy [*Pyles and Froehlich*, 1987]. Air photo analyses can thus be substantially biased toward low landslide densities in forested areas, because a greater proportion of small landslides are missed in forested areas than in unforested areas [*Brardinoni et al.*, 2003; *Robison et al.*, 1999]. However, above a certain size threshold, virtually all landslides are visible on aerial photographs [*Reid and Dunne*, 1996]. Mapping from 1:12,000- and 1:15,000-scale aerial photographs, *Brardinoni et al.* [2003] found these thresholds to be 150 m^2 for landslides in recently clear-cut areas and 650 m^2 in forested areas for field sites in western British Columbia. Mapping from 1:24,000-scale aerial photographs, *Bush et al.* [1997] resolved landslide scars as small as 160 m^2, but estimated the smallest landslide size reliably visible in forested areas as at least 2000 m^2.

[26] Landslide areas obey a negative power law frequency distribution over a large portion of their size range [e.g., *Brardinoni and Church*, 2004; *Hovius et al.*, 1997], thus offering a means for estimating the number of smaller landslides missing from a landslide inventory [*Malamud et al.*, 2004]. The frequency distribution of landslide sizes larger than the visibility threshold provides a relatively unbiased estimate for the large-size portion of the distribution, which can be reliably estimated using landslide inventories from aerial photographs. If we know the shape of the entire frequency distribution, perhaps from a less-biased, field-based inventory [*Brardinoni et al.*, 2003], we can then extrapolate the distribution obtained from the air photo inventory to smaller sizes and estimate the number of small landslides that were missed. The negative power law distribution fits the large-size portion of the distribution well. There is, however, a lower bound to landslide size, so even for inventories considered complete and unbiased, the number of small landslides deviates from the negative power law distribution, producing a rollover effect [*Malamud et al.*, 2004; *Stark and Hovius*, 2001]. *Stark and Hovius* [2001] present a double pareto distribution that describes observed distributions over the full range of landslide sizes:

$$p(s) = \eta\left[\frac{\left(1+\left({}^{m}/_{t}\right)^{-\alpha}\right)^{{}^{\beta}/_{\alpha}}}{\left(1+\left({}^{s}/_{t}\right)^{-\alpha}\right)^{1+{}^{\beta}/_{\alpha}}}\right]\left(\frac{s}{t}\right)^{-\alpha-1}. \tag{15}$$

Here $p(s)$ is the probability density of landslide size s; m is the upper limit of landslide size; α, β, and t are empirical parameters; and

$$\eta = \frac{\beta}{t(1-\delta)},$$

where

$$\delta = \left[\frac{1+\left({}^{m}/_{t}\right)^{-\alpha}}{1+\left({}^{c}/_{t}\right)^{-\alpha}}\right]^{{}^{\beta}/_{\alpha}},$$

with c being the lower limit of landslide size. Values for c and m may be estimated from the smallest and largest landslides included (or expected) in an unbiased inventory. Values for α, β, and t are estimated from the shape of the observed distribution; α corresponds to the exponential decrease in frequency with increasing size for large landslides, β corresponds to the exponentially decreasing frequency with decreasing size for small landslides, and t corresponds to the rollover point where the distribution shifts between these two types.

[27] An empirical probability density of landslide sizes can be estimated for a landslide inventory by plotting $\Delta n(s)/\Delta s$, where $\Delta n(s)$ is the number of landslides with sizes in the increment $s \pm \Delta s/2$. Because there are many more small landslides than large, it is useful to expand the increments with size so that all bins contain some landslides. Values for

α, β, and t can then be adjusted to minimize the absolute difference between the analytic (equation (15)) and empirical density functions. The resulting values can be used in equation (15) with landslide counts from an air photo inventory to estimate the number of landslides missed in the photo mapping for each forest cover class. The number of landslides n in size range s_1 to s_2 is

$$n|_{s_1}^{s_2} = N_T \int_{s_1}^{s_2} p(s)ds, \tag{16}$$

where N_T is the total number of landslides. Using $p(s)$ determined for a field inventory, for example, and the number of landslides counted between sizes s_1 and s_2 from an air photo inventory, we can solve for the total number of landslides N_T in the study area. If either s_1 or s_2 extend into a biased portion of the air photo inventory, where small landslides are undercounted because they are not visible or where the chance of encountering a large landslide is low because there are so few of them, the number of landslides n will be undercounted and N_T will be underestimated. Thus the most unbiased size range for the photo inventory is that giving the maximum estimate for N_T. The correction for the landslide density calculated for the air photo inventory from equation (13) is then

$$\rho = \gamma \rho_{(Photo)}, \tag{17}$$

where ρ is the corrected landslide density, $\rho_{(Photo)}$ is the density measured from the aerial photographs, and γ is the ratio

$$\gamma = N_T / N_C, \tag{18}$$

and N_C is the number of landslides counted in the air photo inventory.

[28] Samples from a population of landslides will exhibit variability in the observed distribution of landslide sizes arising solely from random differences in the number of small and large landslides included in each sample. Some uncertainty therefore arises in the total number of landslides N_T associated with a given number of counted landslides N_C. The magnitude of this uncertainty depends on the shape of the size distribution of the entire population, the probability that a landslide is visible in the photographs, and the number of landslides included in the sample (N_C). We can estimate this uncertainty by approximating the probability that a landslide is visible in a photo using a discrete size threshold. If all landslides larger than a certain size s_V are visible and all smaller are not, then the probability that any single landslide is counted is given by

$$P(visible) = \int_{s_V}^{m} p(s)ds = \frac{1}{\gamma}, \tag{19}$$

where $p(s)$ is the probability density of landslide size, estimated with the double pareto distribution in equation (15), and m is the upper limit of landslide sizes. As indicated in equation (19), the probability that a randomly chosen landslide is counted is given by N_C/N_T, or $1/\gamma$ from equation (18). $P(visible)$ may also be estimated as the proportion of landslides larger than s_V in an unbiased inventory. For a given total number of landslides N_T, to the extent that each has a probability $P(visible)$ of being counted that is a function solely of its size, the probable number counted is described with a binomial distribution, from which uncertainty in N_C may be estimated. The same approach can be used to estimate the uncertainty in N_T associated with a given number N_C of landslides counted. Alternatively, we estimate uncertainty in N_T for a given N_C with Monte Carlo techniques by taking N_T samples with replacement (a bootstrap sample) from a relatively unbiased (e.g., field mapped) inventory and counting landslides larger than s_V to obtain one realization of N_C. Repeated iterations provide an estimated distribution for N_C from which estimates of variability (e.g., variance, confidence intervals) can be obtained.

2.4. Spatial Variability in Landslide Densities

[29] Variability in landslide densities estimated from air photo mapping arises from four sources: spatial variability in the actual landslide density associated with variable terrain and triggering factors, insufficient sample size to average out random variations in landslide spacing, uncertainty in γ (equations (17) and (18)) from random variations in sampled landslide sizes and visibility, and discrepancies introduced by the human mapper [*Ardizzone et al.*, 2002]. Uncertainty in a quantity q, a function of n independent variables x_i, each with their own uncertainty δx_i, can be estimated as [*J. R. Taylor*, 1997]

$$\delta q^2 = \sum \left(\frac{\partial q}{\partial x_i} \delta x_i \right)^2. \tag{20}$$

From equations (17) and (20) we can thus express the uncertainty in $\rho_{(Photo)}$ as

$$\left(\delta \rho_{(Photo)}\right)^2 \approx \frac{1}{\gamma^2}(\delta\rho)^2 + \rho^2 \left(\delta \frac{1}{\gamma}\right)^2 = \frac{1}{\gamma^2}(\delta\rho)^2 + \gamma^2 \rho_{(Photo)}^2 \left(\delta \frac{1}{\gamma}\right)^2, \tag{21}$$

from which we isolate the variability in the corrected landslide density (ρ in equation (17)) as

$$(\delta\rho)^2 \approx \gamma^2 \left[\left(\delta \rho_{(Photo)}\right)^2 - \gamma^2 \rho_{(Photo)}^2 \left(\delta \frac{1}{\gamma}\right)^2 \right]. \tag{22}$$

Using a binomial distribution for N_C, with equation (19) to estimate the probability of successfully seeing a landslide in an aerial photograph, $\delta\gamma$ is proportional to $N_C^{-1/2}$. Estimates for $\delta\rho_{(Photo)}$ and $\rho_{(Photo)}$ are obtained by subsampling (with replacement) over a large study area. An area of given size is delineated on the DEM and the number of mapped landslides within the area counted, from which a single topographically corrected value for $\rho_{(Photo)}$ is obtained with equation (13). These values are then corrected for photo bias using equation (17). Repeated many times, this procedure gives a set of $\rho_{(Photo)}$ values from which to estimate $\delta\rho_{(Photo)}$. Because the distribution of values is positively skewed, we use the median as an estimate of central tendency for $\rho_{(Photo)}$ in equations (21) and (22). Repeated for sampling areas of different size, we see how variability in measured densities changes with the size of

the study area, up to some portion of the total area available for subsampling.

[30] Because of bias in landslide counts, the ratio in landslide density between forested and open (unforested) areas calculated from air photo–based landslide inventories differs from the actual (unbiased) ratio by an amount γ_F/γ_O:

$$\frac{\rho_{F(photo)}}{\rho_{O(photo)}} = \frac{\gamma_O \rho_F}{\gamma_F \rho_O}, \tag{23}$$

where the subscript F refers to forested areas and O refers to open areas. Variability in this ratio arises both from uncertainty in γ_F and γ_O and from variability in the ratio ρ_F/ρ_O. We can estimate the relative contributions as above:

$$\left(\delta\left[\frac{\rho_{F(Photo)}}{\rho_{O(Photo)}}\right]\right)^2 \approx \left(\delta\left[\frac{\gamma_O}{\gamma_F}\right]\right)^2\left(\frac{\rho_F}{\rho_O}\right)^2 + \left(\delta\left[\frac{\rho_F}{\rho_O}\right]\right)^2\left(\frac{\gamma_O}{\gamma_F}\right)^2$$
$$\approx \left(\delta\left[\frac{\gamma_O}{\gamma_F}\right]\right)^2\left(\frac{\gamma_F}{\gamma_O}\right)^2\left(\frac{\rho_{F(Photo)}}{\rho_{O(Photo)}}\right)^2 + \left(\delta\left[\frac{\rho_F}{\rho_O}\right]\right)^2\left(\frac{\gamma_O}{\gamma_F}\right)^2,$$

from which

$$\left(\delta\left[\frac{\rho_F}{\rho_O}\right]\right)^2 \approx \left(\frac{\gamma_F}{\gamma_O}\right)^2\left(\left(\delta\left[\frac{\rho_{F(Photo)}}{\rho_{O(Photo)}}\right]\right)^2 - \left(\delta\left[\frac{\gamma_O}{\gamma_F}\right]\right)^2\left(\frac{\gamma_F}{\gamma_O}\right)^2\left(\frac{\rho_{F(Photo)}}{\rho_{O(Photo)}}\right)^2\right). \tag{24}$$

Subsampling of a study area provides a set of $\rho_{F(Photo)}/\rho_{O(Photo)}$ values from which to estimate both the variability of this ratio and a median value. Values for γ_F and γ_O can be estimated by subsampling with replacement from an unbiased landslide inventory with appropriate lower size cutoffs for landslides visible in forested and open cover classes.

[31] Results provide the range in landslide-density ratios to expect as a function of study area size. This can guide the level of confidence to place in landslide density measurements for a region based on the area encompassed by a study. It also provides the means to develop confidence intervals for the number of landslides predicted with our approach for any delineated area.

3. Model Demonstration

3.1. Study Area

[32] The Oregon Coast Range (Figure 2), extending over approximately 29,000 km^2, is an actively uplifting region [e.g., *Mitchell et al.*, 1994] with a maritime climate characterized by wet winters and occasional long-duration storms [*Taylor and Hannan*, 1999]. It is underlain by shallow water marine sedimentary rocks and scattered basaltic volcanics and intrusives [*Orr et al.*, 1992]. The resulting landscape is of relatively low relief (elevations range from sea level to 1200 m) but highly dissected, with soil-mantled ridge-and-valley terrain of steep slopes. Rainfall-triggered translational landslides of shallow soils that cause debris flows are

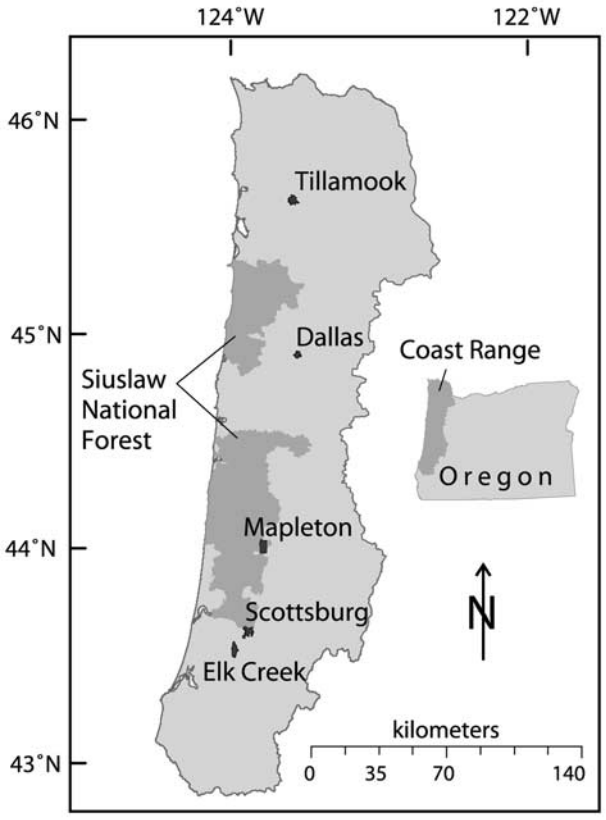

Figure 2. Location of landslide inventories in the Oregon Coast Range. The Siuslaw National Forest (SNF) inventory used aerial photographs taken in the summer of 1996. The Oregon Department of Forestry (ODF) inventory used five sites, including three sites surveyed in the summer of 1996 and the Scottsburg and Elk Creek sites surveyed in the summer of 1997.

a primary process driving sediment flux from upper slopes to valley floors [*Dietrich and Dunne*, 1978], with persistent effects on valley and channel morphology [*Benda*, 1990]. Although not addressed in this study, streamside landslides triggered by bank erosion at slope toes and deep-seated earth-flows [*Roering et al.*, 2005] are other potentially important processes in the region. Both affect stream channels, but a connection with forest disturbance is not as well documented as that for shallow, debris flow–triggering landslides and these other types of landslides have associated topographic characteristics that may differ from the translational landslides we consider.

[33] The Oregon Coast Range is predominately covered by conifer and hardwood forests. Past disturbance regimes included intense, but infrequent, wild fires and windstorms. Current regimes are characterized by extensive timber harvest and fire suppression [*Franklin and Dyrness*, 1988]. These disturbance processes alter the spatial distribution of forest cover classes, and the mean landslide densities we obtain for each class characterize their effects on landslide susceptibility.

3.2. Data

[34] Five data sets were used to demonstrate the modeling approach in the Oregon Coast Range. Three of these span the entire region: (1) a 10-m grid DEM developed from

contours and blue line streams on US Geological Survey 1:24,000-scale digital line graph (DLG) data [*Clarke and Burnett*, 2003]; (2) a vector map of roads, also from US Geological Survey 1:24,000-scale DLG data; and (3) a forest cover classification based on 25-m grid Landsat Thematic Mapper satellite imagery from 1996 in conjunction with topographic, climatic, geologic, and extensive field plot data [*Ohmann and Gregory*, 2002]. Two other data sets, field-based landslide inventories collected by the Oregon Department of Forestry (ODF) [*Robison et al.*, 1999] and an air photo–based landslide inventory collected by the Siuslaw National Forest (SNF) [*Bush et al.*, 1997] span only portions of the Oregon Coast Range (Figure 2).

[35] Forest cover effects on landslide density were explored using the forest cover data set. We grouped the 10 forest cover classes of *Ohmann and Gregory* [2002] into three broad classes approximating those used by the ODF [*Robison et al.*, 1999]: (1) open (<10 yrs age), unforested and recently clear-cut harvested areas, remnant forests, and very-small-diameter (<10 cm diameter at breast height (dbh)) conifer and hardwood/conifer forests; (2) mixed (10–80 yrs), hardwood forests, and small- and medium-diameter (10–50 cm dbh) conifer and hardwood/conifer forests; and (3) large (>80 yrs), large- and very large–diameter (>50 cm dbh) conifer and hardwood/conifer forests. Because the forest cover raster data were of a different resolution than the DEM (25 m versus 10 m), forest classes for each DEM pixel were determined using a nearest-neighbor algorithm. We delineated a 50-m buffer on both sides of all roads in the 1:24,000-scale DLG data. We assumed that this width was sufficient to include all landslides related to the mapped roads and thereby removed them from our analysis of landslide density under forest cover. The DLG data include forest roads visible on the photographs used to construct and update the US Geological Survey topographic maps, but omit old roads that are no longer visible and new roads built after the photos were taken.

[36] The ODF and SNF landslide data sets were collected to capitalize on numerous landslides triggered by intense winter storms in 1996 [*Hofmeister*, 2000], in part to look for differences in landslide density between forest cover classes that reflect the effects of timber harvest. Each landslide data set offered certain benefits. Although landslide locations were mapped on 1:24,000-scale base maps in both studies, the field mapping of ODF included small landslides that were not visible in the aerial photographs, and so provided a relatively unbiased sample of landslide sizes and an accurate measure of stream-affecting landslide densities. The air photo mapping included landslides over a relatively large area, sufficient to obtain regionally applicable values of landslide density by forest class and to analyze spatial variability in measured ratios of landslide density between forest cover classes. With both data sets, we characterized each landslide at the inferred initiation point, rather than over the entire area encompassed by the landslide scar (see discussion by *Dietrich et al.* [2001]), because our goal was to identify conditions likely to be associated with debris flow initiation.

[37] The ODF data set included five sites in the Oregon Coast Range, encompassing a total area of 77 km^2 (Figure 2). These data consisted of two landslide inventories collected through extensive field mapping by the Oregon Department of Forestry (ODF) in the summers of 1996 and 1997 [*Robison et al.*, 1999], following major storms in February and November 1996 [*G. Taylor*, 1997]. Four of these sites were chosen because of the large number of landslides they contained; the Dallas site (Figure 2) was chosen randomly without reference to the number of landslides. Each site encompassed about 15 km^2. The Elk Creek, Scottsburg, and Mapleton sites are within the Tyee formation, a thick sequence of gently dipping sandstone and siltstone beds (map unit Tt of *Walker and MacLeod* [1991]). The other two are in igneous lithologies; the Tillamook site overlies basalts of the Tillamook Volcanics and the Dallas site is predominately within the basaltic Siletz River Volcanics (map units Ttv and Tsr of *Walker and MacLeod* [1991]). At each field site, the ODF attempted to document every landslide that delivered material to stream channels [*Robison et al.*, 1999]. All channels up to 40% gradient were surveyed and any landslide identified in the channel was traced to its source. The ODF collected a variety of information about each landslide, including location and dimensions of the initiating failure and of subsequent runout. Locations were recorded on US Geological Survey 1:24,000-scale base maps and later digitized, with mapped initiation locations stored as points. Landslide initiation locations were also documented using GPS receivers where feasible. We used data only from landslides classified by ODF as 'upslope.' Thus we intentionally omitted landslides triggered by stream undercutting because forest cover and topographic influences on initiation processes for streamside landslides may differ from those that are the focus of this study. The ODF inventory excluded landslides that did not runout to stream channels. We did not view this as constraining our use of these data because we were interested in characterizing landslides that enter stream channels.

[38] The SNF landslide inventory was mapped in March 1996 from 1:24,000-scale color aerial photographs [*Bush et al.*, 1997]. The mapping encompassed approximately 5,665 km^2 of the Oregon Coast Range and included all shallow debris avalanche and debris flow (torrent) landslides, including runout zones, interpreted as associated with the February storm. Of the mapped landslides, 35% reached second- and higher-order streams; of the remainder, some reached first-order streams and some did not, but these were not differentiated in the inventory. Block glide and earth flow landslides were not mapped by the SNF. We manually located initiating points for the 1,320 landslide polygons digitized by the SNF. These polygons were typically long and narrow, ranging from 161 m^2 to 42,238 m^2. Locations of the initiation points were estimated at the head of the landslide scar after considering the landslide polygons overlain with the 1:24,000-scale digital raster graphics of US Geological Survey topographic maps and the hillshade produced from the 10-m DEMs. The initiation points typically fell within one to two pixels below the highest elevation in the landslide polygon.

3.3. Topographic Index and Composite Weighting Term for the ODF Study Sites

[39] To define a composite weighting term (w_T) for the ODF study sites, we first calculated an I_T value for every DEM pixel for all sites using equation (2) (with α = 130 m^2/day

for the Oregon Coast Range, from $T = 65$ m^2/day, $\rho_S = 2000$ kg/m^3, and $\rho_W = 1000$ kg/m^3, taken from *Montgomery et al.* [1998]). Each digitized landslide initiation point in the ODF data set was associated with the pixel having the smallest index value within a radius of 30 m. We obtained a continuous approximation for F_L versus F_A (the number-versus-area curve) using a maximum likelihood fit of a logistic equation to the empirical number-versus-area curve defined by equations (3) and (4), plotted against the logarithm of the topographic index. Derivatives were calculated analytically for the fitted logistic equation to give the numerator and denominator in equation (5), which provided a continuous function $f(I_T)$ (equation (7)).

[40] To extend $f(I_T)$ to a composite weighting function that accommodates different forest cover classes, we started with uncorrected estimates of the mean density (number of landslides divided by area) for ρ_i in equation (12), one for each of the three forest cover classes. The differentials, dn_A/dI_T, were estimated using a second-order polynomial fit over a centered window along the DEM area versus topographic index points. This provided an initial estimate for w_T, which was then used in equation (13) to give an updated estimate of mean landslide density for each forest class. These new mean density values were then used in equation (12), which gave an updated w_T. This new term was used with equation (13) to update the mean density values and the entire process iterated until the estimated mean densities were unchanged between iterations.

[41] To evaluate the ability of the weighting term (w_T) to characterize topographic influences on landslide susceptibility, we compared landslide number-versus-area curves from the ODF field inventory and from 10,000 synthetic inventories generated with Monte Carlo modeling. We did this first with ODF data for all landslide locations combined; these were the data used to obtain the w_T function, so the degree to which the synthetic curves envelope the field data indicate how well our curve fitting techniques reproduce the pattern indicated by the mapped landslide locations. We then grouped landslide locations by forest cover and rock type. In these cases, divergence of the data points from the synthetic curves indicate systematic differences in topographic influences for different forest cover and rock types.

[42] We also compared the synthetic curves obtained with DEMs for the SNF study to data from the SNF air photo inventory to compare topographic controls inferred from field-mapped landslide locations to those inferred from locations mapped on aerial photographs. As done with the ODF data, each digitized initiation point mapped from the SNF inventory was associated with the pixel having the smallest topographic index value within a 30-m radius.

3.4. Landslide Detection Bias in Aerial Photographs

[43] Both the ODF and SNF landslide inventories included measures of landslide size (surface area). We used mean widths and lengths measured by the field teams for the initiating landslide and runout track to obtain a surface area for each landslide in the ODF inventory and used the area encompassed by the digitized polygons for landslides mapped in the SNF inventory. We assume that there is no bias between forest cover types for ground-based landslide counts and so use all landslides in the ODF inventory to estimate the size distribution. For the SNF inventory, we divided landslides into three groups, one for each forest cover type, and estimated size distributions for each separately.

3.5. Spatial Variability in Landslide Densities

[44] We used the SNF air photo inventory to examine how landslide density between different forest cover classes might vary with the area over which it is measured [see also *Miller et al.*, 2003]. We counted landslides within many, randomly placed subsets of the total study area, first using sampled areas entirely within a single forest class, and then for sampled areas that included multiple classes in order to calculate the ratio of densities between forest classes within the sampled area. After correcting for topographic variability and photo bias, this subsampling yielded a range of values of landslide density for each class and for each landslide density ratio (mixed to open, large to open, and large to mixed). We repeated this exercise for different sample area sizes to see how the median value and the width of the 90% confidence intervals changed as the area examined increased. We adjusted these confidence intervals for air photo detection bias (γ) using equation (22) for landslide density and equation (24) for landslide density ratios. By examining differences between the widths of confidence intervals before and after adjustment, we estimated the proportion of the variability in measured values arising from landslides missed on the aerial photos as a function of sample area.

3.6. Roads

[45] Roads are ubiquitous in many forested landscapes and, because roads can affect landslide processes, road-related landslides need to be addressed when determining forest cover influences on landslide density. We exclude road-related landslides from our analyses using a buffer around all mapped roads: DEM pixels and landslides within the buffer are removed from subsequent analyses. However, because available data for road locations in forested areas are often incomplete, some roads may be missed. Effects of undetected roads are implicitly incorporated when assessing spatial variability in landslide densities.

[46] Where roads are mapped, landslide inventory data can be used to assess road effects on landslide density. Landslide counts within the road buffer can be compared to the number of landslides predicted with equation (13). The effects of topography are accounted for in the predicted value through the topographic weighting term. It is not necessary to correct for counting bias between forest cover classes, because comparison is with the number actually counted on the photographs.

4. Results

4.1. Topographic Index and Composite Topographic Weighting Term

[47] All landslides mapped for the five ODF sites were located in DEM pixels with topographic index (I_T) values that encompassed 0.74 of the total area (Figure 3a). The landslide number-versus-area curve obtained from these data and the fitted logistic curve are shown in Figure 3b. The tangent to the logistic curve gives the composite topographic weighting term (w_T, equation (12)) plotted in Figure 3c. The topographic weighting term for these data

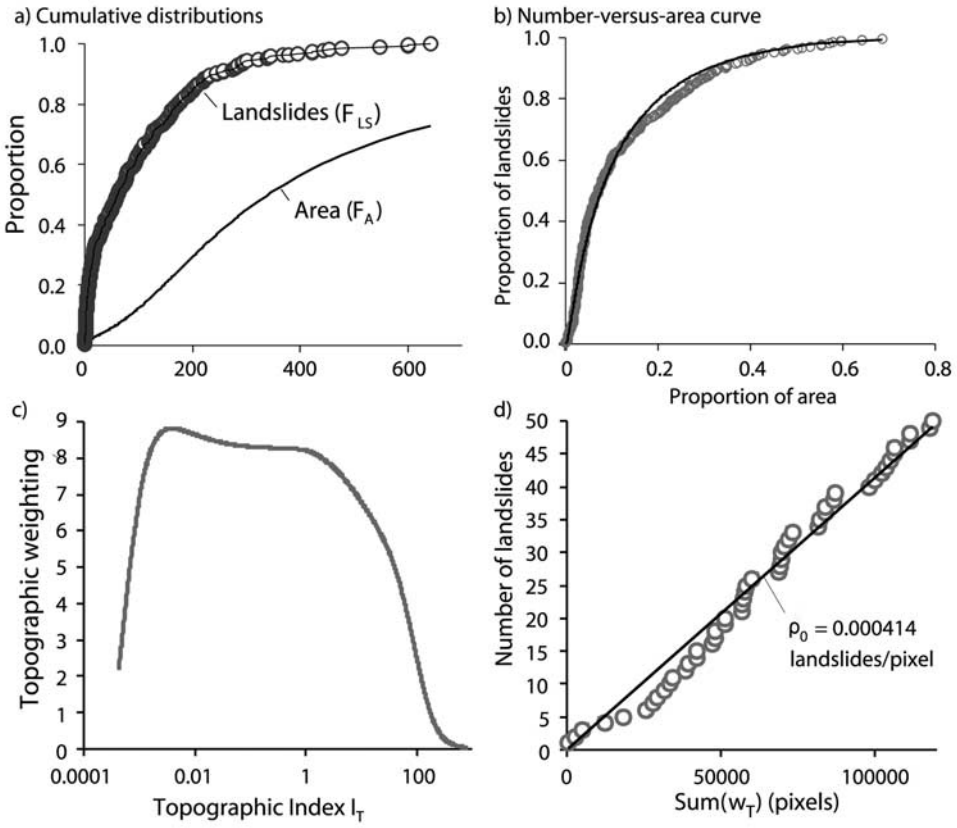

Figure 3. (a) Empirical cumulative distributions for landslides and DEM area versus topographic index I_T for composite data from the five ODF field sites from equations (3) and (4); (b) number-versus-area curve obtained from these data (open circles) and the fit logistic curve (gray line); (c) topographic weighting term obtained from the number-versus-area curve; and (d) plot of the summed topographic weighting value versus mapped number of landslides for the open class at the ODF sites, which from equation (13) gives the mean landslide density.

decreases for the smallest topographic index values, possibly corresponding to hillslopes that are too steep to accumulate soil [*Montgomery and Dietrich*, 1994]. Mean landslide densities for subsets of the study area (e.g., for each forest cover class) were obtained using equation (13), as illustrated for the open forest class in Figure 3d.

[48] The spatial distribution of these I_T and w_T values are shown for the ODF Mapleton study site in Figure 4. As context, Figure 4a provides mapped landslides, forest cover classes, and the road buffer overlain on a DEM hillshade of the study site. Calculated values of the topographic index (Figure 4b) show that small I_T values are concentrated on steep, convergent hillslopes. The topographic weighting term, based on the curve in Figure 3c, is mapped in Figure 4c. High values of w_T, corresponding to higher landslide densities (less stable slopes), are concentrated in steeper and more convergent locations. Curves like that of Figure 3d (from equation (13)) were used iteratively with the topographic weighting function to obtain topographically corrected landslide densities for each forest cover class. Together, the mean landslide densities for each cover class, multiplied by the topographic weighting term, give the distribution of landslide densities shown in Figure 4d.

4.2. Evaluating the Topographic Weighting Term

[49] The performance of the topographic weighting term (w_T) obtained from the entire ODF data set was evaluated first by comparing the landslide number-versus-area curve for all landslides in the ODF field inventory to those obtained from 10,000 synthetic landslide inventories generated with Monte Carlo modeling (Figure 5a). Values in the curves are ranked from least to most stable, so those closer to the origin are associated with less-stable hillslopes. Somewhat fewer landslides than indicated by w_T occur in the least stable zones (low I_T values), indicated by the data points below area proportions around 0.02 that extend slightly below the lower boundary of the 90% confidence interval. Analogously, somewhat more landslides than indicated by w_T occur in intermediate stability zones, near area proportions of 0.05, indicated by data points that extend slightly above the upper boundary of the 90% confidence interval. The logistic curve we used to fit the cumulative distribution cannot reproduce these patterns in the empirical curves, so our resulting model yields a smoothed estimate.

[50] Results obtained when comparing the observed and synthetic number-versus-area curves for each forest cover class separately (Figures 5b–5d) were similar to those for all classes combined (Figure 5a). However, the 90% confidence interval for each forest cover–specific curve was wider than that for all ODF data combined, reflecting the greater variability expected with a smaller sample size. Empirical data for the three forest cover classes were not identically distributed, but all data points fell within the

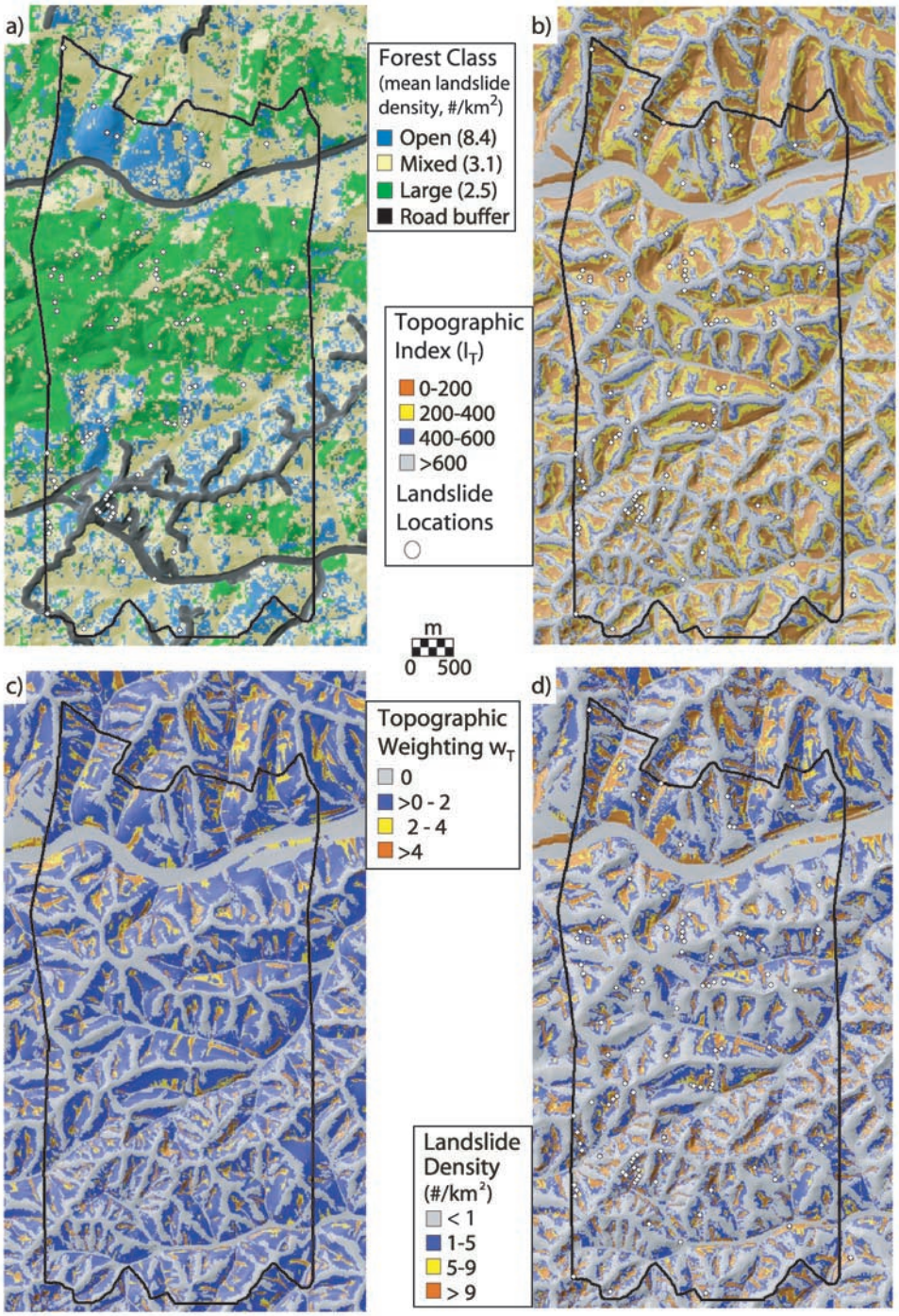

Figure 4. Maps from the ODF Mapleton study site showing the (a) topographic and land cover context for field-mapped landslides, (b) topographic index (I_T), (c) topographic weighting term (w_T), and (d) density of landslide initiation points calculated as the product of the topographic weighting term and the mean landslide density. Study site boundary is indicated by the heavy black line.

range of values obtained with Monte Carlo modeling (Figures 5b–5d).

[51] When the ODF sites were divided by rock type, data points for sandstones (Figure 6a) fell well within the 90% confidence interval curves generated with the weighting term from the full data set. The majority of inventoried landslides were in sandstones, and so this result was not surprising. The data for sites underlain by basaltic volcanics, however, deviated substantially from the generated curves (Figure 6b). Landslides were more concentrated in topography having smaller (less stable) I_T values than indicated by the weighting term, so the model overestimated the area in basalts required to encompass a given proportion of all landslides.

[52] We also compared results of Monte Carlo modeling using the weighting term developed from the ODF study

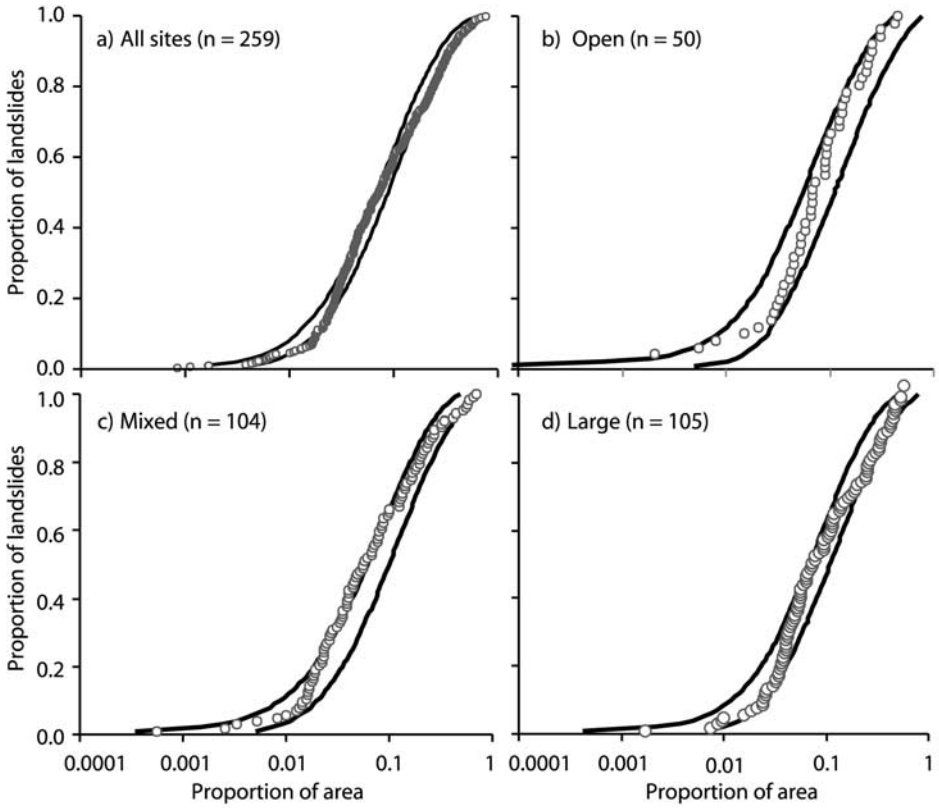

Figure 5. Landslide number versus area curves for (a) composite data from all five ODF study sites and (b) open, (c) mixed, and (d) large forest cover classes. Heavy lines show 90% confidence intervals obtained with Monte Carlo modeling using the composite topographic weighting term shown in Figure 3. Open dots are from mapped landslide initiation point locations. For this and subsequent figures displaying landslide number versus area curves, the proportion-of-area axis is in a logarithmic scale to highlight variability for landslides in the least stable terrain.

sites with number-versus-area curves from the DEMs and air photo–based landslide inventory for the SNF study area. A greater proportion of the mapped landslides fell on hillslopes with larger I_T values (more stable) than predicted by the topographic weighting term (Figure 7) and well outside the 90% confidence interval.

4.3. Landslide Detection Bias in the Air Photo–Based Inventory

[53] Empirical probability densities for landslide sizes in the ODF inventory are plotted in Figure 8, along with those for landslides in each of the three forest cover classes in the SNF inventory. We assume that in each case the landslides from the SNF air photo mapping are from the same underlying size distribution as the ODF field-mapped inventory, but with some unknown proportion of the smaller landslides uncounted. The distributions plotted in Figure 8 support this view. The slope of the curves defined by the data are parallel for both inventories at large landslide sizes, but the curve for each cover class in the SNF data tends to roll over at a larger landslide size and fall off more rapidly with decreasing size than the ODF distribution, with the large cover class having the largest rollover point.

[54] The degree to which landslides were undercounted in each cover class was estimated using equation (16) over a range of upper and lower size bounds (s_1 and s_2). We found that the upper and lower landslide size limits giving the maximum N_T value varied with each forest cover class. The lower and upper limits for the open class were 3,800–12,500 m^2, for the mixed class were 5,800–19,300 m^2, and for the large class were 6,600–21,600 m^2. The resulting N_T/N_C ratios (γ of equations 17 and 18) are listed in Table 1. The proportion of landslides missed by photo mapping ($1 - N_C/N_T$) is estimated as 0.88 for the open class, 0.92 for the mixed class, and 0.97 for the large class.

[55] Uncertainty in the total number of landslides (N_T) based on landslides counted in aerial photographs (N_C) was estimated by plotting N_T versus N_C from sampling with replacement of the ODF inventory for three visibility thresholds: 1,250 m^2, 1,625 m^2, and 2,875 m^2 (Figure 9a). These threshold values give γ values that are similar to those obtained from the landslide size distributions discussed above (Table 1). On the basis of the ODF inventory, these values would exclude 50%, 58%, and 75% of the cumulative landslide area.

[56] Confidence in γ increases with smaller visibility thresholds and with larger landslide counts (Figure 9b). For example, the SNF inventory included 529 landslides in the open forest class. For a visibility threshold of 1,250 m^2, there is an estimated 90% probability that the actual number of landslides is between 4,404 and 5,224, corresponding to an N_T/N_C ratio of 9.1 ± 0.78. The SNF inventory included only 136 landslides in the large cover class. For a visibility

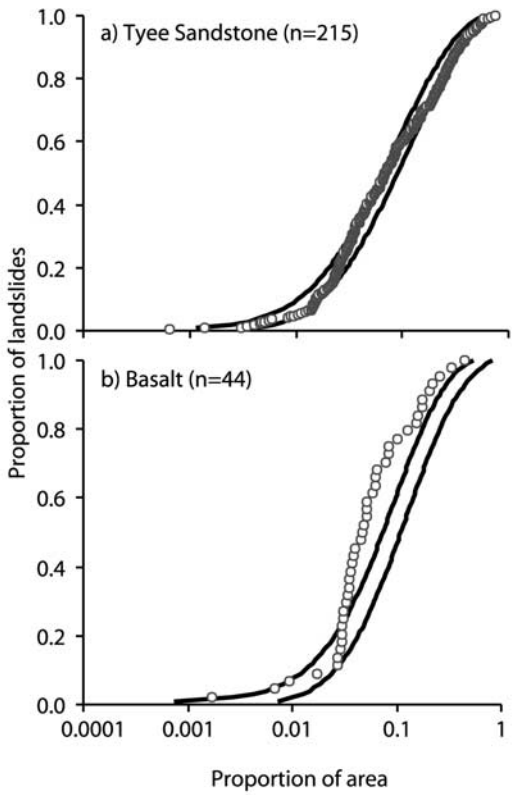

Figure 6. Landslide number versus area curves for the ODF field sites separated by rock type: (a) sandstones and (b) basalts. Heavy lines show 90% confidence obtained with Monte Carlo modeling. Open dots are from mapped landslide initiation point locations.

threshold of 2,875 m^2, there is a 90% probability that the actual number of landslides is between 3,300 and 4,968, corresponding to an N_T/N_C ratio of 30.4 ± 6.1.

4.4. Landslide Density by Forest Cover Class

[57] Using equation (13), mean landslide densities were obtained by forest cover class for all ODF sites combined (Figure 10a) and for each site individually (Figures 10b–10f). Overall, we find the lowest density in the mixed forest class (Figure 10a), consistent with the ODF's interpretation [*Robison et al.*, 1999]. After correcting for topographic differences, however, we found no consistent trend in the relative magnitude of landslide density between forest cover classes among the sites.

[58] For the SNF study area, the mean value of the topographic weighting term over all pixels was 0.53, indicating that a greater proportion of the area has a smaller topographic weighting (more stable) than found in the ODF study sites. The mean value of the weighting term for the ODF sites was 1.0 by definition (from equation (9)), because these provided the calibration data. The mean topographic weighting term for the open class was 0.86 of the mean overall for the SNF study area, the mean for the mixed class was equal to the overall mean, and the mean for the large class was 1.4 times the overall mean. Values less than one indicate terrain that is more stable than the average; values greater than one indicate terrain that is less stable than average. The lower mean weighting value for the open class indicates that these areas tend to fall on lower-gradient, more stable terrain than the mixed and large classes (Table 1). The larger mean weighting for the large class indicates that these areas tend to occupy less stable terrain.

[59] To adjust for bias from interpretation of aerial photographs, landslide densities in each forest cover class were multiplied by the values of γ in Table 1. Adjustments for photo-bias affected calculated landslide densities much more than adjustments for topography, with the largest adjustment applied to the large cover class. After correcting for topographic differences and air photo bias between forest cover classes, results based on the SNF landslide inventory indicate the lowest landslide density in the oldest forests (Table 1).

4.5. Spatial Variability in Landslide Densities

[60] We subsampled over the SNF study area to examine spatial variability in measured landslide density. For a single forest cover class, the median of all nonzero landslide densities obtained from sampling of the SNF inventory decreased with increasing sample area (Figures 11a–11c). This occurred because, at small sampling sizes, a significant number of samples include no landslides, so the nonzero samples are biased toward larger values [*Miller et al.*, 2003]. As the sample area increases, beyond some point all samples contain landslides and the median is constant with increasing sample area. This occurs at about 20 km^2 for the open class, about 50 km^2 for the mixed class, and between 75 and 100 km^2 for the large class. The range of densities also decreased with increasing sample area, shown by the width of the envelope containing 90% of all sampled values (Figure 11).

[61] From equations 21 and 22, we divide the range in densities between uncertainty in γ, representing variability in air photo bias, and uncertainty in landslide density ρ, representing variability in average landslide spacing (from e.g., variations in rainfall intensity). The proportion of this range arising from uncertainty in γ is substantial at small sample areas, decreases with increasing sample area, and becomes negligible for areas greater than about 10 km^2

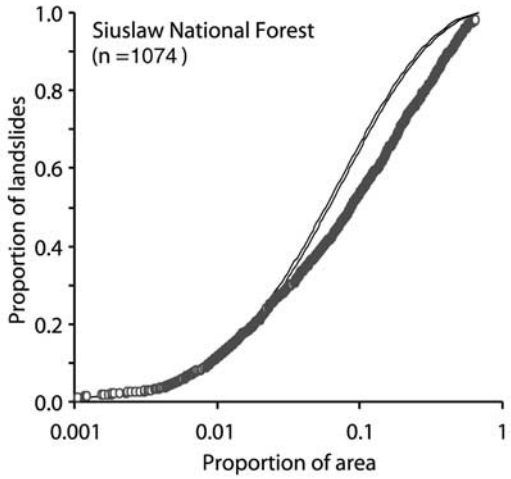

Figure 7. Landslide number versus area curves for the Siuslaw National Forest landslide inventory. Solid lines show 90% confidence intervals obtained with Monte Carlo modeling using the topographic weighting term (Figure 3) obtained from the ODF field sites. Open dots from mapped landslide initiation point locations.

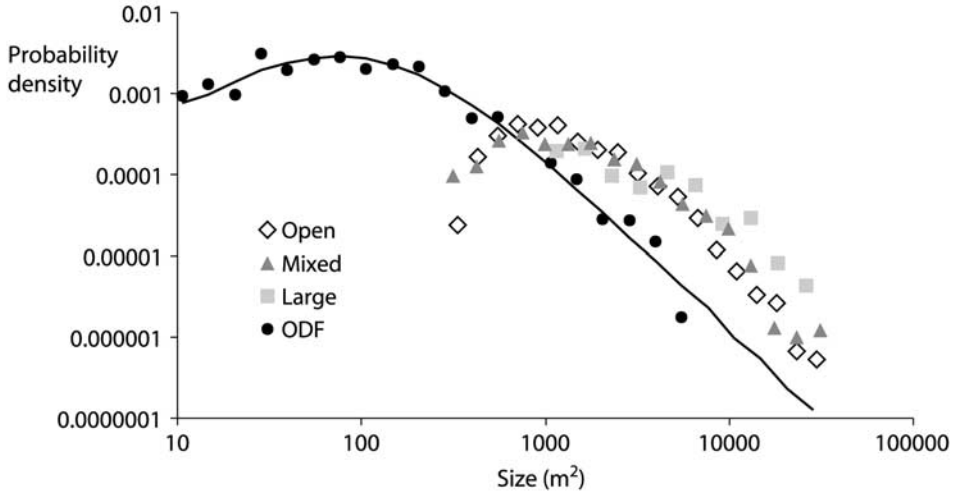

Figure 8. Landslide size distributions, given in probability density ((number in bin/total number)/bin width), for each forest cover class in the Siuslaw inventory and for all landslides in the ODF inventory. Solid line shows a double pareto distribution, equation (15), fit to the ODF data.

(Figures 11d–11f). The remaining variability in landslide density ρ is relatively constant and substantial across all sample areas (Figures 11d–11f). For each forest cover class, the width of the 90% confidence interval (after accounting for uncertainty in γ) is about 2.3 times the median value.

[62] We also subsampled the SNF study area to examine variability in the ratio of landslide densities between forest cover classes within a sample area. For a set of samples of equal specified area, the area in each forest cover class varied among samples depending on where the samples were located. We sampled over a range of areas from 10 to 1,000 km^2 and took 10,000 randomly placed samples for each size increment. The smallest sample size was larger than that used previously, because each sample contains multiple forest cover classes, whereas in the previous example each sample contained only a single forest cover class. Samples for both the large-to-mixed and large-to-open ratios had median values that decreased and 90% confidence intervals that narrowed as the area of the sample increased, converging to the values obtained for the study area as a whole (Figures 12a and 12b). The proportion of the range of landslide densities arising from uncertainty in γ is relatively constant across the range of sample areas examined, entailing about 15% of the variability in the large-to-open ratio and about 33% of the variability in the large-to-mixed ratio. The remaining variability in ratio values is still substantial, but decreases with increasing sample area (Figures 12c and 12d).

[63] A curious aspect in comparing landslide densities between forest classes is that results typical for small areas can contradict those obtained over larger areas. Excluding areas with no landslides, the large forest cover class typically had more landslides per unit area than the mixed cover class, indicated by a large-to-mixed ratio exceeding one (Figure 12a). It is only at sample areas exceeding 500 km^2 that the median value of the sampled ratios drops below 1.0.

4.6. Roads

[64] For each forest cover type, we found more landslides than predicted within the 50-m buffer on either side of mapped roads (Table 2). The ratio of number of landslides mapped to number predicted within the buffer ranged from 1.9 to 3.2, suggesting that the presence of mapped roads at least doubled the probability of landslide initiation. If desired, we can then estimate the effect of roads by multiplying the mean landslide density for each cover class by these ratios within a 50-m buffer of all mapped roads.

[65] Areas within the buffer for roads had a mean topographic weighting equal to 0.53 that of the overall mean for the SNF study area, showing that roads tend to lie in lower-gradient, more stable areas than found on average over the DEM. This result is crucial to our assessment of road effects: without accounting for the topographic location of roads, we would predict landslide numbers twice as large (Table 2).

5. Discussion

5.1. Topographic Influences on Landslide Density

5.1.1. Topographic Index

[66] Although our topographic index was based on the model of *Montgomery and Dietrich* [1994], other indices that characterize topographic influences on slope stability may also be used. Examples include slope gradient and the product of slope gradient and local curvature (a measure of convergence), which lack dependence on contributing area,

Table 1. Results for Siuslaw National Forest Landslide Inventory

Forest Class	Open	Mixed	Large
Area, km^2	671	1592	1219
Number of mapped landslides (n_{LS})	529	409	136
Mean topographic weighting ($\overline{w_T}$)	0.858	1.013	1.358
Photo-detection bias (γ)	9.1	12.4	30.4
Uncorrected landslide density, number/km^2	0.788	0.257	0.112
Topographically corrected density n_{LS}/(Area * $\overline{w_T}$)	0.918	0.254	0.082
Topo and photo-corrected density γ * n_{LS}/(Area * $\overline{w_T}$)	8.4	3.1	2.5

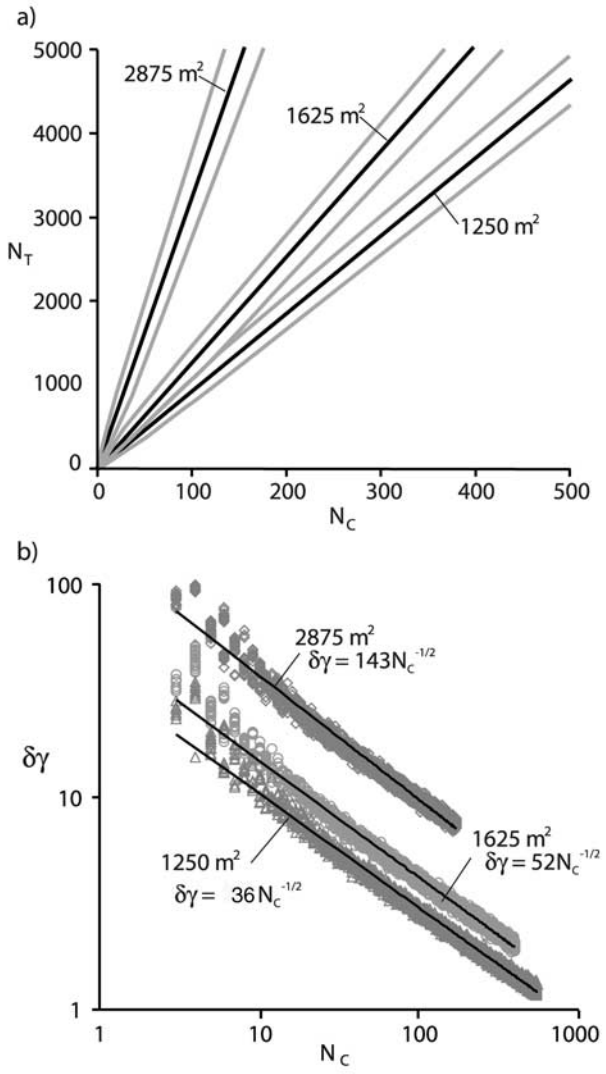

Figure 9. (a) Total number of landslides N_T (black lines), with 90% confidence intervals (gray lines), versus the number counted N_C based on sampling with replacement from the ODF landslide inventory for three visibility thresholds and (b) width of the 90% confidence intervals for γ, the ratio N_T/N_C, for each of these thresholds.

but can perform better in some situations [*Reid et al.*, 2001], potentially depending, for example, on the nature of the triggering storms [*Wieczorek*, 1987]. Our general approach of calibrating an index against landslide mapping and DEMs provides the means to compare topographic influences captured by different indices, landslide inventories (e.g., field mapped versus air photo–mapped landslide locations), or elevation data (e.g., 10-m versus 30-m DEMs). The greater the proportion of landslides captured in a given proportion of area, expressed in landslide number-versus-area curves (e.g., Figures 5–7), the better the index, inventory, or elevation data is at resolving topographic controls.

5.1.2. Landslide Initiation Points

[67] Each landslide in the ODF inventory was characterized in terms of a single topographic index value at the inferred initiation point. However, some uncertainty surrounds which DEM pixel represents the landslide initiation point, arising both from the level of precision available from mapping on 1:24,000-scale base maps and from ambiguity as to where within a landslide scar the failure initiated. We therefore chose the least stable DEM pixel (lowest index value) within a specified radius of the mapped point. Our choice of 30 meters for this radius was based on the assumption that a 1.25 mm margin (the extent of 30 m on a 1:24,000-scale map) adequately represented the uncertainty in the mapped landslide initiation point on the base map. The radius selected influences the resulting distribution of index values associated with landslides. As the radius increases, the distribution shifts to less stable values [*Dietrich et al.*, 2001], thereby changing the shape of the number-versus-area curves and the resulting topographic weighting term. It is important therefore that the same radius be used to compare results between sites.

[68] Likewise, any bias in the placement of initiation points, such as our choice to locate points near the highest elevations enclosed by the SNF landslide polygons, also affects inferred relationships with topography. Although our procedures were systematic and well documented, differences among studies in techniques for placing initiation points will confound attempts to compare results relating landslides and topography.

[69] Our findings suggest that field mapping more precisely characterized landslide locations than air photo mapping for the data sets we used. This is indicated by the divergence of the number-versus-area curve for the photo-mapped landslide locations from curves predicted with a topographic weighting term derived from the field mapped locations (Figure 7). Such a pattern could result if landslide initiation points mapped from the aerial photographs were likely to be misplaced onto adjacent points on the hillslopes with higher topographic index (I_T) values, either during the mapping or the digitizing processes. This is particularly likely for landslides within a topographic hollow, the axis of which has much lower topographic index values than adjacent areas. Likewise, smaller landslides, which tend to be missed on the aerial photographs, provide greater precision in locating initiation points simply because initiation points are chosen from a smaller landslide scar. The pattern we observed in the number-versus-area curves may also have arisen if smaller landslides occurred in different topographic locations than larger landslides. In any case, the field-mapped locations better resolved topographic controls on landslide location, and thus provided a more reliable weighting term than obtained from air photo mapping.

5.1.3. Topographic Weighting Term

[70] In evaluating the performance of the topographic weighting term (w_T), the logistic function we fit to the cumulative distribution (Figure 3a) for all landslides in the ODF field inventory generated a smoothed estimate, and so the modeled curves were not identical to the empirical data (Figures 3b and 5a). A different function with additional degrees of freedom may better fit the shape of the empirical curve. However, we were reluctant to try matching every inflection, given uncertainties regarding the signal-to-noise ratio of these data. We thought that the smooth form of the logistic curve provided a good compromise; the empirical data fell within the range of values obtained with a weighting term derived from the tangent to the logistic curve.

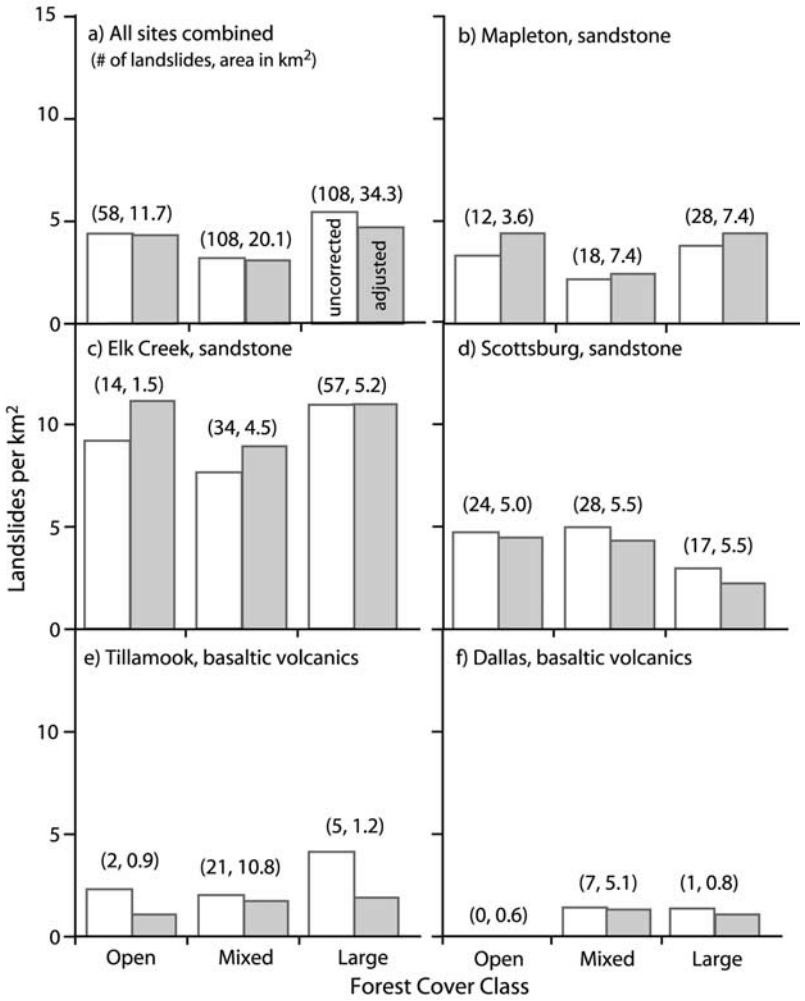

Figure 10. Mean landslide densities for each forest cover class (a) for composite data from all five ODF sites combined and (b–f) for each site individually. White bars show uncorrected landslide density; gray bars show landslide density adjusted for topographic variability between forest cover classes at each site. The number of landslides and area (km^2) in each class are in parentheses.

[71] The number-versus-area curves for the mapped landslides shown in Figure 5 differed slightly among the forest cover classes, but 90% confidence intervals generated by Monte Carlo modeling indicated that all fell within the likely range obtained with a single composite weighting term. A larger sample may resolve significant differences between forest cover classes, if they exist. However, we think that the currently available data do not justify the added complexity of separate weighting terms for each forest cover class.

[72] Landslide locations in the Tyee sandstone were well characterized with the composite topographic weighting term, but those in basalts were less so, as shown in Figure 6. This suggested that a separate weighting term for basalts might be warranted. However, we considered data from the ODF field inventory insufficient to divide landslide points by both forest cover class and rock type given that only 44 landslides were sampled in basalts. We therefore decided to combine data across rock types, increasing the number of landslides for calculating the composite topographic weighting term and thus increasing overall confidence in our estimates. As a consequence, this improved the model for regional application, but landslide densities in specific locations may be overestimated. For applications limited to basalts, obtaining additional landslide data and calibrating a specific topographic weighting term is advisable.

[73] In part, our use of a single topographic weighting term across different forest cover classes and geologic units is driven by our desire for a simple model that can be implemented across large areas. Use of a single weighting term allows us to calculate a single topographic weighting value for each pixel, stored as a raster file. We then multiply this raster file by the mean landslide density to obtain a spatially distributed estimate of landslide susceptibility (Figure 4d). The mean landslide density is obtained from GIS coverages of forest cover, categorized into our open, mixed, and large classes, each with its own landslide density (Table 1). This strategy provides a straightforward assessment of topographic influences on landslide susceptibility, given by the raster file of topographic weighting terms for each DEM pixel, and a method for rapid assessment of forest cover influences on landslide susceptibility. It is certainly feasible, however, to develop a more detailed model using separate topographic weighting terms calibrated to specific terrain units, which may be appropriate for other types of model applications.

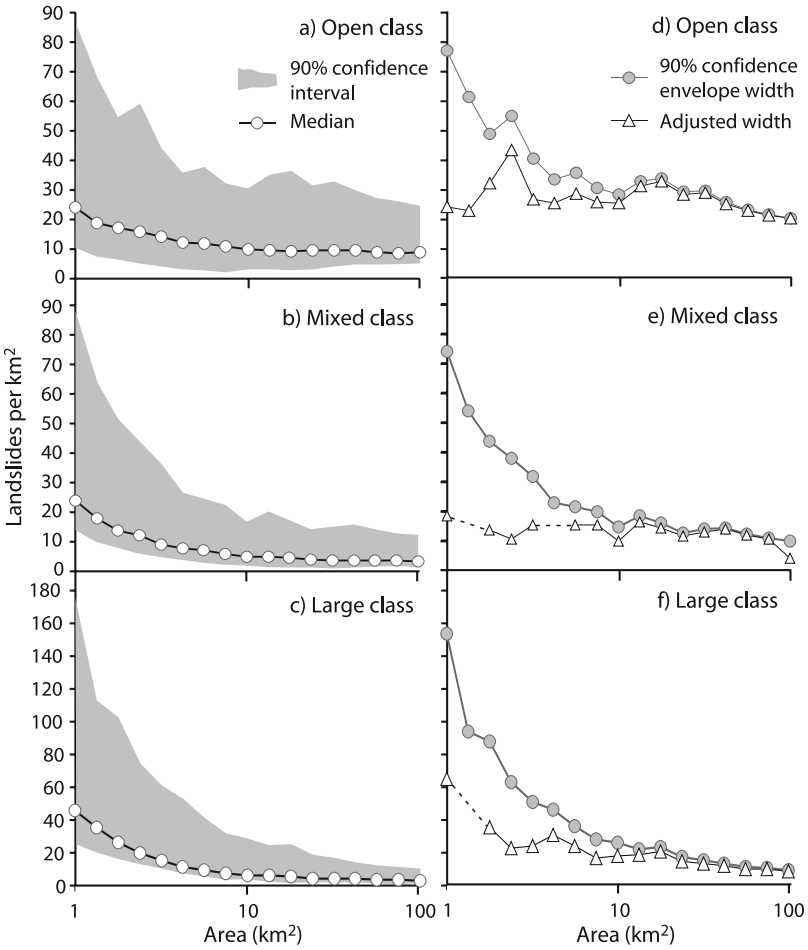

Figure 11. Variation in landslide density with sample size over the SNF study area. Shown are median and 90% confidence intervals of landslide density for subsamples from 1 to 1000 km^2 for (a) open, (b) mixed, and (c) large forest cover classes. Also shown is width of the 90% confidence interval from the sampled values before and after adjustment for uncertainty in air photo detection bias (γ) (equation (22)) for (d) open, (e) mixed, and (f) large forest cover classes; differences between the curves for the 90% confidence width and the adjusted width represent the variability due to uncertainty in detection bias.

[74] Differences in mean topographic weighting among forest cover classes may reflect the history of timber harvests in the region. Logging of steep slopes requires specialized equipment and costs more than timber harvest in lower-gradient areas; thus harvested areas (open and mixed classes) tend to occupy more stable terrain (lower mean topographic weighting values) than unharvested areas (large class). Likewise, it is less expensive to build and maintain roads on lower-gradient, stable terrain than on steep, unstable slopes; thus roads tend to occupy areas with low topographic weighting values. This is an important point when comparing landslide densities near roads to densities found for hillslope areas.

5.1.4. Storm Effects

[75] Topographic locations for rainfall-triggered landslides can differ with storm characteristics, such as intensity and duration [*Wieczorek*, 1987]. Our topographic weighting is calibrated to landslides triggered by two storms: the February event was of high-intensity and long duration; the November event was generally of higher intensity and shorter duration. Calibration to landslides from a different set of storms may have altered the performance of the topographic index and lead to a different value for the topographic weighting term. The large number of landslides triggered by the 1996 storms motivated field and air photo studies that provided an informative data set, but comparison with landslide locations from other events is needed to fully determine the generality of our results.

5.2. Bias in Aerial Photographs

[76] Our estimates of the degree to which landslides were undercounted on aerial photographs were substantial and differed by forest cover class. We determined that undercounting of landslides was greater in forested than in nonforested areas. This is consistent with direct comparisons of landslide counts between ground-based inventories and air photo–based inventories for the Oregon Coast Range using 1:6000-, 1:12,000-, and 1:24,000-scale photos [*Robison et al.*, 1999] and for coastal British Columbia, Canada using 1:12,000- and 1:15,000-scale photos [*Brardinoni et al.*, 2003].

[77] Regional assessments of landslide susceptibility rely primarily on analysis of aerial photographs that yield biased estimates of landslide density by forest cover class. The simplest method to address such bias is restricting analysis to one forest cover class, e.g., open areas. This was the approach taken by *Rollerson et al.* [2002], which is suffi-

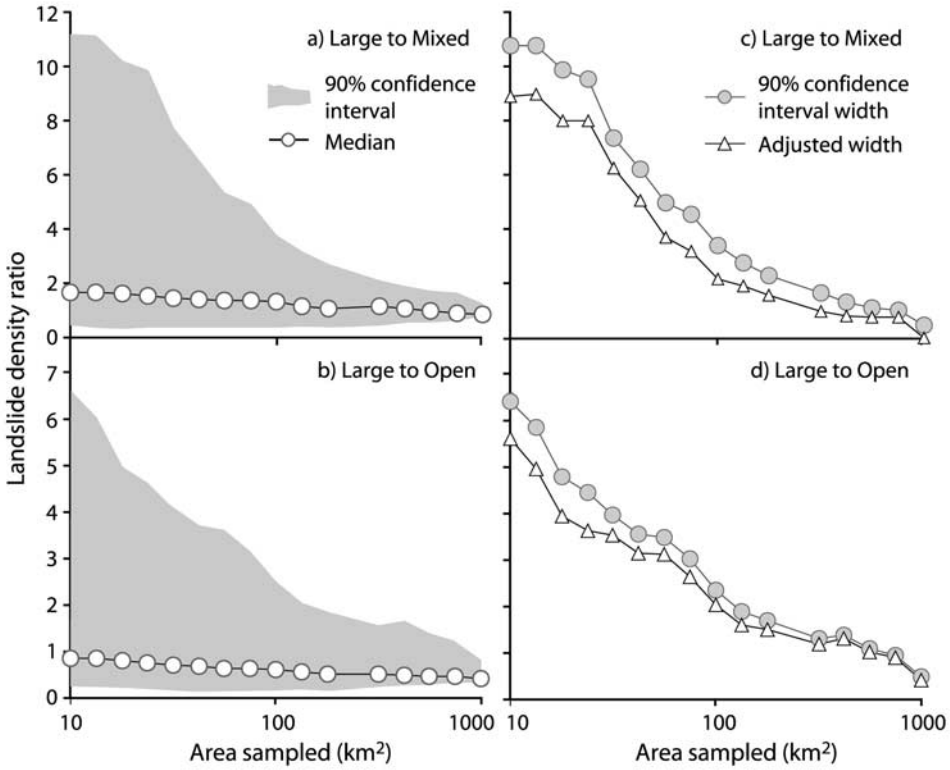

Figure 12. Variation in the ratio of landslide densities with sample size over the SNF study area. Shown are median and 90% confidence intervals for the ratio of landslide density between the (a) large and mixed classes and (c) large and open forest cover classes. Also shown is width of the 90% confidence interval from the sampled values before and after adjustment for uncertainty in air photo detection bias (γ) (equation (24)) for (b) large to mixed and (d) large to open ratios; differences between the curves for the 90% confidence width and the adjusted width represent the variability due to uncertainty in detection bias.

cient for identifying terrain attributes associated with landsliding after timber harvest but cannot address the effects of logging on landslide density. In contrast, our strategy, based on comparing landslide size distributions, estimates the bias in density measurements for different forest cover classes and the uncertainty around these estimates. Thus we provide the means to consider the effects of forest disturbance on landslide density.

[78] Our strategy is, however, based on the assumptions that we are comparing field- and air photo–based landslide inventories from the same underlying size distribution and that no other sources of bias exist in the samples. These assumptions could not be rigorously evaluated in our analysis. For example, the ODF inventory included only landslides that traveled to stream channels, of which we excluded streamside landslides, whereas the SNF inventory included all shallow landslides visible on the photos, some of which may not have traveled to stream channels. However, data are not available to determine if landslide sizes in the two inventories represent the same or different underlying populations. Additionally, the SNF inventory followed one major storm, whereas the ODF inventory contained data that were collected after this and another storm. We assumed that the distribution of landslide sizes is unchanged with storm characteristics. This is consistent with the observation that landslide inventories from a variety of locations exhibit similar size scaling relationships [*Malamud et al.*, 2004], but is unverified in our case. Ideally, future data collection protocols will seek to minimize potential sources of bias and analytical techniques will be developed to better evaluate underlying assumptions.

5.3. Landslide Density by Forest Cover Class

[79] After correcting for topographic variability and detection bias in aerial photograph mapping, we found distinct differences in landslide density between forest cover classes in the SNF landslide inventory, with the highest average density in recently disturbed areas (open class) and the lowest density in older forests (large class) (Table 1). This result emerged only when landslide density was

Table 2. Results for Road Buffer

Forest Class	Open	Mixed	Large	All
Area in buffer, km^2	135	448	173	756
Summed topographic weighting ($\sum w_T$), km^2	63	234	104	401
Landslide density (ρ from Table 1), number/km^2	0.918	0.254	0.082	0.308
Number of landslides mapped	112	126	29	267
Number of landslides predicted ($\rho \sum w_T$)	58	59	9	124
Number mapped/number predicted	1.9	2.1	3.2	2.2
Number predicted with no topographic correction (ρ area)	124	114	14	232

evaluated over fairly large areas (>500 km^2); over smaller areas, older forests typically contained more landslides per unit area than younger forests (mixed class) as we and *Robison et al.* [1999] observed for the ODF field sites (Figure 10a). Such an outcome is possible if landslides tend to be more clumped in the large forest class and more evenly distributed in the open and mixed classes. If so, a greater proportion of sampled areas would include no landslides in the large class [*Miller et al.*, 2003]. Accordingly, since we excluded samples with no landslides, higher densities were observed in the large class for smaller sample areas. The same can be expected when field inventories are purposely focused in areas containing landslides, which is common.

[80] Although we had insufficient data to examine differences in landslide density associated with variability in rock type or storm characteristics, our approach can still resolve relative differences in landslide density between forest cover classes. This is true as long as variability in forest cover occurs over smaller spatial extents than variability in rock type and storm characteristics. By using the cumulative distribution functions (equations (3) and (4)) to define topographic effects, in which the proportion of landslides are associated with a proportion of area, calibration of the weighting term is unaffected by spatial variations in landslide density. Therefore, even if the absolute landslide density varies with rock type or storm characteristics, as long as the ratio in mean landslide density between forest cover classes is the same in each case, the relative difference in density between forest classes is constant. This aspect was of particular importance to our analysis, because data were lacking on variations in intensity and duration of the 1996 storms and to constrain landslide densities in rock types other than sandstones. If or how much landslide density ratios vary in different situations remains an issue to be resolved.

[81] Estimates of landslide density translate directly to estimates of the probability that a landslide was mapped within any specific area on the landscape, a DEM pixel for example (equation 14). These estimates are subject to the constraints of the calibration data, which in this study reflected landslides associated with two large storm events in a single year. This precluded using this calibration for estimating landslide rates (number per unit area per unit time). However, to the extent that landslides triggered by these storms manifest characteristics of landslide locations associated with other storms, the available data provide a spatially distributed estimate of the relative probability for landslide occurrence, i.e., where landslides are most and least likely to originate.

[82] Point-to-point differences in modeled landslide densities reflect the relative effect of topography and forest cover. If relative landslide densities between forest cover classes do not vary substantially with location or time, then we can use the model to estimate differences in the relative number of landslides associated with changes in forest cover. This provides the ability to evaluate effects of past and current timber harvest on current and future patterns of landslide susceptibility.

5.4. Spatial Variability

[83] The ODF and SNF landslide inventories exhibited great site-to-site variability in relative landslide density between forest cover classes. This suggests that forest cover effects on landslide density (and any rates inferred from those densities) must be estimated over broad spatial extents to be reliably extrapolated regionally. Field-based landslide inventories, because they can include the full range of landslide sizes, are generally viewed as better indicators of landslide density in forested areas than are air photo inventories. Our results support this view (e.g., Figure 9), but also indicate that field-based estimates of landslide density must be interpreted in light of potential variability over the spatial extent of the field study. As shown by the 90% confidence intervals in Figure 12, a high probability exists that relative densities measured over tens of square kilometers will contradict those measured over hundreds of square kilometers. The time and effort required often limit field surveys to relatively small areas, tens of square kilometers; whereas dramatic differences in landslide densities between study sites (Figures 10 and 12) suggest that much larger sample areas are required to obtain regionally applicable averages. For results that represent regional averages, landslide densities must be compared among forest cover classes over large areas, typically necessitating the use of air photo analyses. This does not preclude the need for careful field mapping, which can help to compensate for the potentially poorer resolution and bias inherent in mapping from aerial photographs.

5.5. Roads

[84] The 1:24,000 DLG data for the study area incompletely represent road locations and omit information on other attributes that can influence landsliding (e.g., road type, age, and level of use and maintenance). Although we attempted to remove all road-related landslides from the SNF database, some were undoubtedly retained and influenced our estimates of landslide densities for the three forest cover classes. This was another source of variability in measured landslide densities that we could not constrain. However, the effects of roads on landslide density were indirectly incorporated in our analysis of variability.

[85] Although incomplete mapping of roads is an issue in most places this modeling approach may be applied, the effects of mapped roads on landslide densities can be accounted for. Our approach accomplishes this within a 50-m buffer on either side of all mapped roads by multiplying the mean landslide density for each forest class by the factors in Table 2. For example, in recently harvested areas (open forest class), the mean landslide density applied within 50 m of any road would be 1.9 times greater than the mean density applied elsewhere (Table 2, line 6); in mature forests (large forest class) the mean density applied within 50 m of roads would be 3.2 times greater than elsewhere. This provides an estimate, based on observations over a 5,665 km^2 area, of road effects averaged across road type, age, and level of maintenance.

6. Conclusions

[86] Motivated by a need to assess the geomorphic and ecological implications of timber harvest on susceptibility to debris flow initiation, we developed methods using widely available data (10-m DEMs, landslide inventories, and forest cover mapping) to estimate effects of topography, forest cover, air photo detection bias, and spatial variability on the density (number per unit area) of rainfall-triggered translational landslides and for specifying the confidence to

place in those estimates. These methods rely on both field- and air photo–based landslide inventories, which used together capitalize on the strengths and overcome the deficiencies in each data source. Topographic influences on landslide susceptibility are inferred at the DEM resolution, providing a GIS-based model with sufficient detail to identify individual debris flow source areas and with sufficient data coverage to apply over large regions (e.g., the 29,000 km^2 Oregon Coast Range).

[87] Our approach estimates and adjusts for uncertainty in forest cover–specific landslide densities arising from topographic variability and from detection bias in aerial photographs. We found that regional estimates of landslide densities among forest cover classes were affected less by adjusting for differences in topography than for differences in visibility of landslides on aerial photographs. The ability to account for air photo bias is therefore critical when examining landslide densities under different forest cover classes to evaluate logging effects on landslide initiation. However, topographic effects cannot be ignored. Without accounting for topography, for example, we could not accurately assess the effect of roads on landslide density (Table 2).

[88] For the data we used, differences in landslide density between forest cover classes varied considerably among sample sites and the range of values varied with the size of the area sampled. After accounting for topographic variability, we found no consistency among sites in field-based estimates of landslide density under different forest covers. After correcting for both topographic variability and air photo bias, subsampling an air photo–based landslide inventory demonstrated that relative landslide densities measured over small areas may contradict those measured over large areas. In samples encompassing tens of square kilometers, older forests tended to contain the highest landslide densities; for samples encompassing hundreds of square kilometers (>500 km^2), all samples had the lowest landslide densities under older forests.

[89] The methods presented here can be used to estimate the number of initiation sites for translational landslides expected over any delineated area, to look at how that number might change with a change in forest cover, and to specify the confidence to place in those results. Because the model uses regionally available data, we can extrapolate these results over the entire Oregon Coast Range. Predictions are predicated on the data used for calibration. In this study, data were from a series of two intense storms, so we cannot infer landslide rates, but we can infer differences in susceptibility to landslide initiation during a large storm for different locations and under different forest cover classes. As new landslide inventories and better DEMs become available, the model can be evaluated and updated. These methods can be applied anywhere similar data are available and potentially adapted to accommodate different types of data and other types of landslide processes.

Notation

Topographic weighting

I_T Topographic index.

F_{LS} Empirical cumulative distribution function of landslides ranked by topographic index.

F_A Empirical cumulative distribution function of DEM area ranked by topographic index.

n_{LS} Number of landslide-containing pixels.

n_A Number of DEM pixels.

f Rate of change along the F_{LS} versus F_A curve with a change in topographic index.

f_p Value of F within a single DEM pixel.

ρ_0 Mean landslide density (number per unit area).

w_T Topographic weighting term, a function of topographic index.

Topographic index

q_{cr} Critical steady state rainfall intensity for failure of thin, cohesionless soil in *Montgomery and Dietrich* [1994] model, used here as topographic index.

T Soil transmissivity.

θ Ground surface gradient, degrees.

ρ_S Wet bulk density of soil, kg/m^3.

ρ_W Density of water, kg/m^3.

a Contributing area, m^2.

b Unit contour length, m.

ϕ Friction angle of soil, degrees.

C $T(\rho_S/\rho_W)$.

Landslide size distribution

s Landslide size, m^2.

$p(s)$ Probability density of landslide size, double pareto distribution.

m Maximum landslide size, m^2.

c Minimum landslide size, m^2.

t Rollover point in landslide size distribution, m^2.

α, β Parameters in double pareto distribution used for landslide sizes.

Aerial photograph mapping bias

N_T Actual number of landslides.

N_C Number counted in photograph.

s_V Lower size threshold for landslides visible on photograph, m^2.

$P(visible)$ Probability that a landslide is larger than s_V.

ρ On-the-ground landslide density, number per unit area.

$\rho_{(Photo)}$ Landslide density determined from aerial photograph, number per unit area.

γ Ratio $\rho/\rho_{(Photo)}$, equal to N_T/N_C.

[126] **Acknowledgments.** This research was conducted as part of the Coastal Landscape Analysis and Modeling Study (CLAMS) [*Spies et al.*, 2007]. Financial support for this work was provided by the USDA Forest Service Pacific Northwest Research Station and Earth Systems Institute. We thank the Siuslaw National Forest and the Oregon Department of Forestry for assistance in obtaining and interpreting their landslide inventory data. George Bush with the SNF and Jim Paul with the ODF were both particularly helpful. We also thank the three anonymous reviewers whose comments and suggestions helped greatly in our presentation of this material.

References

Ardizzone, F., M. Cardinali, A. Carrara, F. Guzzetti, and P. Reichenbach (2002), Impact of mapping errors on the reliability of landslide hazard maps, *Nat. Hazards Earth Syst. Sci.*, *2*, 3–14.

Benda, L. E. (1990), The influence of debris flows on channels and valley floors in the Oregon Coast Range, U.S.A., *Earth Surf. Processes Landforms*, *15*, 457–466.

Benda, L. E., and T. W. Cundy (1990), Predicting deposition of debris flows in mountain channels, *Can. Geotech. J.*, *27*, 409–417.

Benda, L., K. Andras, D. Miller, and P. Bigelow (2004), Confluence effects in rivers: Interactions of basin scale, network geometry, and disturbance regimes, *Water Resour. Res.*, *40*, W05402, doi:10.1029/2003WR002583.

Borga, M., G. Fontana, C. Gregoretti, and L. Marchi (2002), Assessment of shallow landsliding by using a physically based model of hillslope stability, *Hydrol. Processes*, *16*, 2833–2851.

Brardinoni, F., and M. Church (2004), Representing the landslide magnitude-frequency relation: Capilano River Basin, British Columbia, *Earth Surf. Processes Landforms*, *29*, 115–124, doi:10.1002/esp.1029.

Brardinoni, F., O. Slaymaker, and M. A. Hassan (2003), Landslide inventory in a rugged forested watershed: A comparison between air-photo and field survey data, *Geomorphology*, *54*, 179–196.

Brenning, A. (2005), Spatial prediction models for landslide hazards: Review, comparison and evaluation, *Nat. Hazards Earth Syst. Sci.*, *5*, 853–862.

Burroughs, E. R. J., and B. R. Thomas (1977), Declining root strength in Douglas-fir after felling as a factor in slope stability, *Res. Pap. INT-190*, 27 pp., For. Serv., U.S. Dep. of Agric., Odgen, Utah.

Bush, G., C. McConnel, C. Cloyd, K. Musser, B. Metzger, and H. Plumley (1997), Assessment of the effects of the 1996 flood on the Siuslaw National Forest, report, 47 pp., For. Serv., U.S. Dep. of Agric., Corvallis, Oreg.

Cenderelli, D. A., and J. S. Kite (1998), Geomorphic effects of large debris flows on channel morphology at North Fork Mountain, eastern West Virginia, USA, *Earth Surf. Processes Landforms*, *23*, 1–19.

Chen, J. C., and C. D. Jan (2003), Probabilistic equation of critical slope for debris-flow occurrence, in *Debris-Flow Hazards Mitigation: Mechanics, Prediction, and Assessment*, edited by D. Rickenmann and C. Chen, pp. 83–89, Millpress, Rotterdam, Netherlands.

Chung, C. J., and A. G. Fabbri (2003), Validation of spatial prediction models for landslide hazard mapping, *Nat. Hazards*, *30*, 451–472.

Chung, C. J., and A. G. Fabbri (2005), Systematic procedures of landslide-hazard mapping for risk assessment using spatial prediction models, in *Landslide Hazard and Risk*, edited by T. Glade, M. G. Anderson, and M. J. Crozier, pp. 139–174, John Wiley, Hoboken, N. J.

Clarke, S., and K. Burnett (2003), Comparison of digital elevation models for aquatic data development, *Photogramm. Eng. Remote Sens.*, *69*, 1367–1375.

Coe, J. A., J. W. Godt, R. L. Baum, R. C. Bucknam, and J. A. Michael (2004), Landslide susceptibility from topography in Guatemala, in *Landslides: Evaluation and Stabilization*, edited by W. Lacerda et al., pp. 69–78, Taylor and Francis, Philadelphia, Pa.

Collins, B. D., and G. R. Pess (1997), Evaluation of forest practices prescriptions from Washington's Watershed Analysis program, *J. Am. Water Resour. Assoc.*, *35*, 969–996.

Dengler, L., A. K. Lehre, and C. J. Wilson (1987), Bedrock geometry of unchannelized valleys, in *Erosion and Sedimentation in the Pacific Rim*, edited by B. Beschta et al., pp. 81–90, IAHS Press, Washington, D. C.

Dietrich, W. E., and T. Dunne (1978), Sediment budget for a small catchment in mountainous terrain, *Z. Geomorphol.*, *29*, 191–206.

Dietrich, W. E., D. Bellugi, and R. R. de Asua (2001), Validation of the shallow landslide model, SHALSTAB, for forest management, in *Land Use and Watersheds: Human Influence on Hydrology and Geomorphology in Urban and Forest Areas*, *Water Sci. Appl. Ser.*, vol. 2, edited by M. S. Wigmosta and S. J. Burges, pp. 195–227, AGU, Washington, D. C.

Dunne, T. (1998), Critical data requirements for prediction of erosion and sedimentation in mountain drainage basins, *J. Am. Water Resour. Assoc.*, *34*, 795–808.

Franklin, J. F., and C. T. Dyrness (1988), *Natural Vegetation of Oregon and Washington*, 464 pp., Oreg. State Univ. Press, Corvallis.

Gershenfeld, N. (1999), *The Nature of Mathematical Modeling*, 344 pp., Cambridge Univ. Press, New York.

Gesch, D., M. Oimoen, S. Greenlee, C. Nelson, M. Steuck, and D. Tyler (2002), The National Elevation Dataset, *Photogramm. Eng. Remote Sens.*, *68*, 5–11.

Gomi, T., R. C. Sidle, and J. S. Richardson (2002), Understanding processes and downstream linkages of headwater systems, *BioScience*, *52*, 905–916.

Guzzetti, F., A. Carrara, M. Cardinali, and P. Reichenbach (1999), Landslide hazard evaluation: A review of current techniques and their application in a multi-scale study, central Italy, *Geomorphology*, *31*, 181–216.

Guzzetti, F., M. Cardinali, P. Reichenbach, and A. Carrara (2000), Comparing landslide maps: A case study in the Upper Tiber River Basin, central Italy, *Environ. Manage.*, *25*, 247–263, doi:10.1007/s002679910020.

Hack, J. T., and J. C. Goodlett (1960), Geomorphology and forest ecology of a mountain region in the central Appalachians, *U.S. Geol. Surv. Prof. Pap.*, *347*, 66 pp.

Hammond, C., D. Hall, S. Miller, and P. Swetik (1992), Level 1 Stability Analysis (LISA) documentation for version 2.0, *Gen. Tech. Rep. INT-285*, 190 pp., Intermountain Res. Stn., U.S. For. Serv., U.S. Dep. of Agric., Ogden, Utah.

Hartman, G. F., J. C. Scrivener, and M. J. Miles (1996), Impacts of logging in Carnation Creek, a high-energy coastal stream in British Columbia, and their implication for restoring fish habitat, *Can. J. Fish. Aquat. Sci.*, *53*, 237–251.

Hicks, B. J., J. D. Hall, P. A. Bisson, and J. R. Sedell (1991), Responses of salmonids to habitat changes, in *Influences of Forest and Rangeland Management on Salmonid Fishes and Their Habitats*, edited by W. R. Meehan, pp. 483–518, Am. Fish. Soc., Bethesda, Md.

Hofmeister, R. J. (2000), Slope failures in Oregon: GIS inventory for three 1996/97 storm events, *Spec. Pap. 34*, 20 pp., Oreg. Dep. of Geol. and Min. Ind., Portland.

Hovius, N., C. P. Stark, and P. A. Allen (1997), Sediment flux from a mountain belt derived by landslide mapping, *Geology*, *25*, 231–234.

Hovius, N., C. P. Stark, C. Hao-Tsu, and L. Juin-Chuan (2000), Supply and removal of sediment in a landslide-dominated mountain belt: Central Range, Taiwan, *J. Geol.*, *108*, 73–89, doi:10.1086/314387.

Iverson, R. M. (2000), Landslide triggering by rain infiltration, *Water Resour. Res.*, *36*, 1897–1910.

Iverson, R. M., M. E. Reid, and R. G. LaHusen (1997), Debris-flow mobilization from landslides, *Annu. Rev. Earth Planet. Sci.*, *25*, 85–138.

Keim, R. F., and A. E. Skaugset (2003), Modelling effects of forest canopies on slope stability, *Hydrol. Processes*, *17*, 1457–1467, doi:10.1002/hyp.5121.

Kelsey, H. M. (1980), A sediment budget and an analysis of geomorphic process in the Van Duzen River basin, north coastal California, 1941–1975: Summary, *Geol. Soc. Am. Bull.*, *91*, 190–195.

Lamberti, G. A., S. V. Gregory, L. R. Ashkenas, R. C. Wildman, and K. M. S. Moore (1991), Stream ecosystem recovery following a catastrophic debris flow, *Can. J. Fish. Aquat. Sci.*, *48*, 196–208.

Malamud, B. D., D. L. Turcotte, F. Guzzetti, and P. Reichenbach (2004), Landslide inventories and their statistical properties, *Earth Surf. Processes Landforms*, *29*, 687–711.

Mark, R. K., and E. B. Newman (1988), Rainfall totals before and during the storm: Distribution and correlation with damaging landslides, *U.S. Geol. Surv. Prof. Pap.*, *1434*, 17–26.

May, C. L. (2002), Debris flows through different forest age classes in the central Oregon Coast Range, *J. Am. Water Resour. Assoc.*, *38*, 1–17.

May, C. L., and R. E. Gresswell (2003), Processes and rates of sediment and wood accumulation in headwater streams of the Oregon Coast Range, USA, *Earth Surf. Processes Landforms*, *28*, 409–424.

May, C. L., and R. E. Gresswell (2004), Spatial and temporal patterns of debris-flow deposition in the Oregon Coast Range, USA, *Geomorphology*, *57*, 135–149.

Miller, A. J. (1990), Fluvial response to debris associated with mass wasting during extreme floods, *Geology*, *18*, 599–602.

Miller, D. J., and L. E. Benda (2000), Effects of punctuated sediment supply on valley-floor landforms and sediment transport, *Geol. Soc. Am. Bull.*, *112*, 1814–1824.

Miller, D. J., C. H. Luce, and L. E. Benda (2003), Time, space, and episodicity of physical disturbance in streams, *For. Ecol. Manage.*, *178*, 121–140.

Mitchell, C. E., P. Vincent, R. J. Weldon, and M. Richards (1994), Present-day vertical deformation of the Cascadia margin, Pacific Northwest, United States, *J. Geophys. Res.*, *99*, 12,257–12,277.

Montgomery, D. R. (1999), Process domains and the river continuum, *J. Am. Water Resour. Assoc.*, *35*, 397–410.

Montgomery, D. R., and W. E. Dietrich (1994), A physically based model for the topographic control on shallow landsliding, *Water Resour. Res.*, *30*, 1153–1171.

Montgomery, D. R., K. Sullivan, and H. M. Greenberg (1998), Regional test of a model for shallow landsliding, *Hydrol. Processes*, *12*, 943–955.

Montgomery, D. R., K. M. Schmidt, H. M. Greenberg, and W. E. Dietrich (2000), Forest clearing and regional landsliding, *Geology*, *28*, 311–314.

Nakamura, F., F. J. Swanson, and S. M. Wondzell (2000), Disturbance regimes of stream and riparian systems: A disturbance-cascade perspective, *Hydrol. Processes*, *14*, 2849–2860.

Nehlsen, W., J. E. Williams, and J. A. Lichatawich (1991), Pacific salmon at the crossroads: Stocks at risk from California, Oregon, Idaho, and Washington, *Fisheries*, *16*, 4–21.

Niemann, K. O., and D. E. Howes (1991), Applicability of digital terrain models for slope stability assessment, *ITC J.*, *3*, 127–137.

Ohmann, J. L., and M. J. Gregory (2002), Predictive mapping of forest composition and structure with direct gradient analysis and nearest neighbor imputation in coastal Oregon, USA, *Can. J. For. Resour.*, *32*, 725–741.

Oregon Department of Forestry (2006), Oregon administrative rules, division 623: Shallow, rapidly moving landslides and public safety, Salem.

Orr, E. L., W. N. Orr, and E. M. Baldwin (1992), *Geology of Oregon*, 4th ed., 254 pp., Kendall/Hunt, Dubuque, Iowa.

Pabst, R. J., and T. A. Spies (2001), Ten years of vegetation succession on a debris-flow deposit in Oregon, *J. Am. Water Resour. Assoc.*, *37*, 1693–1708.

Pyles, M. R., and H. A. Froehlich (1987), Discussion of "Rates of landsliding as impacted by timber management activities in northwestern California," by M. Wolfe and J. Williams, *Bull. Assoc. Eng. Geol.*, *24*, 425–431.

Reeves, G. H., L. E. Benda, K. M. Burnett, P. A. Bisson, and J. R. Sedell (1995), A disturbance-based ecosystem approach to maintaining and restoring freshwater habitats of evolutionarily significant units of anadromous salmonids in the Pacific Northwest, in *Evolution and the Aquatic Ecosystem: Defining Unique Units in Population Conservation, American Fisheries Society Symposium 17*, edited by J. L. Nielson and D. A. Powers, pp. 334–349, Am. Fish. Soc., Bethesda, Md.

Reid, L. M., and T. Dunne (1996), *Rapid Construction of Sediment Budgets for Drainage Basins*, 160 pp., Catena, Cremlingen, Germany.

Reid, M. E., S. D. Ellen, D. L. Brien, J. de la Fuente, J. N. Falls, B. G. Hicks, and T. E. Koler (2001), Comparison of topographic models for predicting debris-slide locations, *Eos Trans. AGU*, *82*(47), Fall Meet. Suppl., Abstract H22G-09.

Reneau, S. L., W. E. Dietrich, D. J. Donahue, A. J. T. Jull, and M. Rubin (1990), Late Quaternary history of colluvial deposition and erosion in hollows, central California Coast Ranges, *Geol. Soc. Am. Bull.*, *102*, 969–982.

Rice, S. P., M. T. Greenwood, and C. B. Joyce (2001), Macroinvertebrate community changes at coarse sediment recruitment points along two gravel bed rivers, *Water Resour. Res.*, *37*, 2793–2803.

Robison, G. E., K. A. Mills, J. Paul, L. Dent, and A. Skaugset (1999), Storm impacts and landslides of 1996: Final report, *For. Pract. Tech. Rep. 4*, 145 pp., Oreg. Dep. of For., Salem.

Roering, J. J., K. M. Schmidt, J. D. Stock, W. E. Dietrich, and D. R. Montgomery (2003), Shallow landsliding, root reinforcement, and the spatial distribution of trees in the Oregon Coast Range, *Can. Geotech. J.*, *40*, 237–253.

Roering, J. J., J. W. Kirchner, and W. E. Dietrich (2005), Characterizing structural and lithologic controls on deep-seated landsliding: Implications for topographic relief and landscape evolution in the Oregon Coast Range, USA, *Geol. Soc. Am. Bull.*, *117*, 654–668, doi:10.1130/B25567.1.

Rollerson, T. P., T. Millard, and B. Thomson (2002), Using terrain attributes to predict post-logging landslide likelihood on southwestern Vancouver Island, *For. Res. Tech. Rep. TR-015*, 15 pp., B. C. Minist. of For., Nanaimo, Canada.

Schmidt, K. M., J. J. Roering, J. D. Stock, W. E. Dietrich, D. R. Montgomery, and T. Schaub (2001), The variability of root cohesion as an influence on shallow landslide susceptibility in the Oregon Coast Range, *Can. Geotech. J.*, *38*, 995–1024.

Sidle, R. C., and H. Ochiai (2006), *Landslides: Processes, Prediction, and Land Use*, *Water Resour. Monogr. Ser.*, vol. 18, 312 pp., AGU, Washington, D. C.

Sidle, R. C., A. J. Pearce, and C. L. O'Loughlin (Eds.) (1985), *Hillslope Stability and Land Use*, *Water Resour. Monogr. Ser.*, vol. 11, 140 pp., AGU, Washington, D. C.

Soeters, R., and C. J. van Westen (1996), Slope instability recognition, analysis, and zonation, in *Landslides, Investigation and Mitigation, Transportation Research Board, National Research Council, Special Report 247*, edited by A. K. Turner and R. L. Schuster, pp. 129–177, Natl. Acad. Press, Washington, D. C.

Spies, T. A., K. N. Johnson, K. M. Burnett, J. L. Ohmann, B. C. McComb, G. H. Reeves, P. Bettinger, J. D. Kline, and B. Garber-Yonts (2007), Assessing forest policies in the coastal province of Oregon: An overview of biophysical and socio-economic responses, *Ecol. Appl.*, in press.

Stark, C. P., and H. Hovius (2001), The characterization of landslide size distributions, *Geophys. Res. Lett.*, *28*, 1091–1094.

Swanson, F. J., and C. T. Dyrness (1975), Impact of clearcutting and road construction on soil erosion by landslides in the western Cascade Range, Oregon, *Geology*, *3*, 393–396.

Swanson, F. J., L. E. Benda, S. H. Duncan, G. E. Grant, W. F. Megahan, L. M. Reid, and R. R. Ziemer (1987), Mass failures and other processes of sediment production in Pacific Northwest forest landscapes, in *Streamside Management: Forestry and Fishery Interactions*, edited by E. O. Salo and T. W. Cundy, pp. 9–38, Inst. of For. Resour., Univ. of Wash., Seattle.

Tarboton, D. G. (1997), A new method for the determination of flow directions and upslope areas in grid digital elevation models, *Water Resour. Res.*, *33*, 309–319.

Taylor, G. (1997), Causes of the flood and a comparison to other climate events, in *The Pacific Northwest Floods of February 6–11, 1996: Proceedings of the Pacific Northwest Water Issues Conference*, edited by A. Laenen and J. D. Ruff, pp. 3–7, Am. Inst. of Hydrol., St. Paul, Minn.

Taylor, G. H., and C. Hannan (1999), *The Climate of Oregon: From Rain Forest to Desert*, 211 pp., Oreg. State Univ. Press, Corvallis.

Taylor, J. R. (1997), *An Introduction to Error Analysis: The Study of Uncertainties in Physical Measurements*, 2nd ed., 327 pp., Univ. Sci., Sausalito, Calif.

U.S. Department of Agriculture and U.S. Department of the Interior (1994), *Standards and Guidelines for Management of Habitat for Late-Successional and Old-Growth Forest Related Species Within the Range of the Northern Spotted Owl, Attachment A to the Record of Decision for Amendments to Forest Service and Bureau of Land Management Planning Documents Within the Range of the Northern Spotted Owl*, Portland, Oreg.

van Westen, C. J., N. Rengers, and R. Soeters (2003), Use of geomorphological information in indirect landslide susceptibility assessment, *Nat. Hazards*, *30*, 399–419.

Walker, G. W., and N. S. MacLeod (1991), Oregon geology, map, 2 sheets, scale 1:500,000, Geol. Surv. U.S. Dep. of the Inter., Reston, Va.

Washington Department of Natural Resources (2005), Chapter 222-10, in *Washington Administrative Code: State Environmental Policy Act Guidelines*, pp. 10.1–10.2, Wash. Dep. of Nat. Resour., Olympia.

Wieczorek, G. F. (1984), Preparing a detailed landslide-inventory map for hazard evaluation and reduction, *Bull. Assoc. Eng. Geol.*, *21*, 337–342.

Wieczorek, G. F. (1987), Effect of rainfall intensity and duration on debris flows in central Santa Cruz Mountains, California, in *Debris Flows/Avalanches: Process, Recognition, and Mitigation*, edited by J. E. Costa and G. F. Wieczorek, pp. 93–104, Geol. Soc. of Am., Boulder, Colo.

Wieczorek, G. F., E. L. Harp, R. K. Mark, and A. K. Bhattacharyya (1988), Debris flows and other landslides in San Mateo, Santa Cruz, Contra Costa, Alameda, Napa, Solano, Sonoma, Lake, and Yolo counties, and factors influencing debris-flow distribution, *U.S. Geol. Surv. Prof. Pap.*, *1434*, 133–162.

Wohl, E. E., and P. P. Pearthree (1991), Debris flows as geomorphic agents in the Huachuca Mountains of southeastern Arizona, *Geomorphology*, *4*, 273–292.

Wu, T. H. (1996), Soil strength properties and their measurement, in *Landslides, Investigation and Mitigation, Transportation Research Board, National Research Council, Special Report 247*, edited by A. K. Turner and R. L. Schuster, pp. 319–336, Natl. Acad. Press, Washington, D. C.

K. M. Burnett, Pacific Northwest Research Station, Forest Service, U.S. Department of Agriculture, Corvallis, OR 97331, USA.

D. J. Miller, Earth Systems Institute, Seattle, WA 98107, USA. (danmiller@earthsystems.net)